Journal of Manufacturing Processes 173 (2026) 799–816

Contents lists available at ScienceDirect

Journal of Manufacturing Processes

journal homepage: www.elsevier.com/locate/manpro

Geometry-driven hole-aware adaptive infill for improved tensile performance of FFF components

Andrea Montalti[a,*], Taichi Yamashita[b], Taiyo Nakamura[b], Alfredo Liverani[a], Akihiro Takezawa[b]

[a] Department of Industrial Engineering, Alma Mater Studiorum University of Bologna, Bologna, Italy
[b] Department of Applied Mechanics and Aerospace Engineering, School of Fundamental Science and Engineering, Waseda University, Tokyo, Japan

GRAPHICAL ABSTRACT

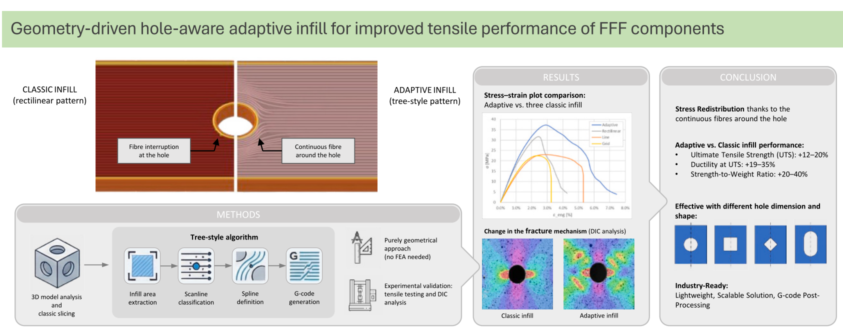

ARTICLE INFO

Keywords:
Material extrusion
Adaptive infill
Hole-aware toolpath
Mechanical anisotropy
Digital image correlation

ABSTRACT

Fused Filament Fabrication (FFF) components exhibit pronounced mechanical anisotropy because filaments are deposited layer by layer along prescribed paths. This anisotropy becomes especially critical in components containing holes, where geometric stress concentration and interruption of load-oriented filaments coexist. This work proposes a geometry-driven hole-aware adaptive infill strategy that aligns deposition paths with the tensile load direction while locally deviating them to preserve path continuity around the hole. Infill lines are treated as virtual structural fibres, thereby reducing path interruption in the most critical region.

A purely geometric algorithm based only on slicing information and load direction was developed without preliminary numerical simulations. The strategy was experimentally validated through tensile tests on polymeric FFF specimens with central holes of different sizes and shapes and compared with conventional slicer-generated infills. Relative to the best conventional baseline, the adaptive infill increased ultimate tensile strength by 12–20% and strain at maximum load by 19–35%, while elastic modulus changed only moderately (1–3%). Absorbed energy and specific strength were also enhanced.

Digital Image Correlation showed a modified fracture mechanism, with delayed crack propagation from the hole due to the locally reinforced path arrangement. The results demonstrate that hole-aware, load-aligned path continuity can improve the mechanical performance of FFF components through a slicing-compatible workflow without increasing material usage or requiring simulation-driven planning.

* Corresponding author.
E-mail address: andrea.montalti8@unibo.it (A. Montalti).

https://doi.org/10.1016/j.jmapro.2026.06.075
Received 9 April 2026; Received in revised form 25 June 2026; Accepted 26 June 2026
Available online 8 July 2026

1. Introduction

Components manufactured by Material Extrusion (MEX), and in particular by Fused Filament Fabrication (FFF), exhibit a pronounced anisotropy that arises from the intrinsic nature of the process, which relies on filament deposition along predefined toolpaths and on the superposition of discrete layers. This characteristic leads to a strong dependence of mechanical properties on the deposition direction [1], introducing significant challenges when the component is subjected to structural loads [2].

Two main strategies have emerged in the literature to address this limitation. The first approach aims at reducing anisotropy, seeking to achieve a mechanical behaviour as close as possible to isotropic and to approximate the performance attainable through conventional manufacturing processes [3]. The second approach, which is adopted in the present work, instead exploits the intrinsic anisotropy [4] of the process to enhance performance along the load direction, achieving benefits that are difficult to replicate with other manufacturing technologies.

In an FFF component, three main features can be identified as contributors to structural strength: infill, perimeters, and top/bottom layers [5]. Several studies have demonstrated that each of these features plays a relevant role in the overall mechanical behaviour of the component [6,7].

Croccolo et al. [8] highlighted the structural importance of perimeters, showing that an increase in their number leads to a significant improvement in mechanical performance. This effect is attributable to the fact that filaments oriented parallel to the load direction operate under particularly favourable conditions [9]. Consistent results have been confirmed by other experimental investigations reported in the literature [10,11].

A similar behaviour has been observed for top/bottom layers [12], for which both analytical analyses and experimental studies have demonstrated the influence of deposition angle and layer count on component stiffness and strength.

Infill, however, represents the most influential feature, as it constitutes the majority of the component volume. Parameters such as density, pattern, and deposition angle [13] play a decisive role in determining the global mechanical response [5,14]. Numerous studies have focused on identifying optimal combinations of these parameters in order to maximize the strength-to-weight ratio, one of the primary advantages of FFF-manufactured components [10,15]. Samykano et al. [16,17] and Rodríguez-Panes et al. [18] identified optimal configurations among the patterns and densities available in mainstream conventional slicers.

Other works have analysed a broader set of printing parameters using Design of Experiments (DOE) approaches [19] or systematic experimental campaigns [20], with the aim of identifying the most effective trade-offs for performance maximization [21]. More recently, machine-learning-based methods [14,22] have been proposed to predict optimal configurations, significantly reducing the number of required experimental tests. Some studies have instead focused on reducing internal voids to increase strength [23], a strategy also adopted at the industrial level, for example in the Stratasys patent based on brick-layer deposition [24].

When optimization of standard parameters is no longer sufficient, it becomes necessary to design advanced infill patterns [25]. Continuous sparse infill frameworks have also been proposed to guarantee uninterrupted toolpaths over geometrically complex interior domains, thereby reducing crossovers and stop–start defects [26,27]. In this direction, variable-density infills [28], including gradient distributions [29] or sandwich architectures [15,30], have been proposed, as well as combinations of different patterns along the build direction, as demonstrated by Aboelella et al. [31], with the aim of reinforcing critical regions induced by geometry or loading conditions. Related work has shown that globally continuous hybrid paths can connect contour and zigzag segments into a single printable trajectory, improving continuity even in domains with holes and complex inner boundaries [32,33].

Even more complex patterns include bio-inspired or organic structures [34,35], lattice structures [36], and architectures obtained through topology optimization [37], which enable performance levels beyond those achievable through traditional parameter optimization alone.

Finally, some authors have proposed strategies based on stress maps [38,39]. These typically involve analysing principal stress directions [40,41] obtained from numerical simulations [42,43], which are then exploited to define optimized deposition paths [44]. Although effective, such approaches require a complex and computationally expensive numerical simulation phase, which is justifiable only for highly specialized applications.

Recent developments show that the design of deposition trajectories is increasingly treated as a structural problem rather than as a simple selection among conventional infill presets. In polymeric material extrusion, optimized or field-oriented toolpaths have been proposed to improve load transfer through path organisation, including optimized material-extrusion planning [38], principal-stress-direction-aware streamlined paths [40], stress-driven infill mapping [42], load-dependent path planning [43], and non-planar alignment of extrusion with stress vectors [44]. These studies demonstrate the mechanical potential of path design, but they generally rely on stress-field evaluation, optimization loops, or non-standard planning frameworks, thus limiting their direct transfer to routine polymer-only FFF practice [45].

A second aspect, directly relevant to the present work, concerns the stress concentration generated by holes and the way in which this interacts with filament interruption in FFF components. The stress distribution in a holed plate under tensile loading was first analysed by Kirsch (1898) and subsequently extended to finite plates and non-circular geometries. These classical solutions describe stress concentration as a purely geometric effect under the assumption of a mechanically continuous material [46].

In FFF-manufactured components, a hole similarly induces a stress peak at the geometric discontinuity [47,48]. However, the classical description becomes insufficient because the material continuity implicitly assumed in analytical and numerical solutions is not preserved at the filament level [49]. In conventional slicing strategies, deposition lines are interrupted whenever a perimeter is encountered; consequently, load-oriented filaments are systematically terminated at the hole boundary [50,51].

This interruption of filaments represents a fundamental departure from the continuum assumption and plays a critical role in the mechanical response of FFF components [52,53]. The stress concentration is therefore not only governed by geometry, but is effectively amplified by the loss of filament continuity [54,55] precisely in the region of maximum stress. As a result, damage initiation and fracture [56,57] are promoted at the hole boundary [58] beyond what would be expected from geometric considerations alone.

Against this background, the studies most closely related to the present problem can be broadly grouped into two families. The first comprises toolpath-planning methods for material extrusion and FFF in which deposition paths are aligned with mechanically relevant directions or optimized fields [38,40,59–61]. The second comprises open-hole or discontinuity-aware strategies developed mainly for continuous-fibre systems, where fibre steering, continuous path generation, and simulation-assisted design are used to preserve load transfer around holes [62–67]. Table 1 summarizes the most relevant studies with respect to the present contribution.

From the standpoint of standard polymer-only FFF, a specific gap remains. A practical strategy is still missing for generating load-aligned infill around internal discontinuities using only slicing information and nominal load direction, without preliminary numerical simulations, without continuous-fibre hardware, and without substantial changes to conventional slicing workflows. This gap is particularly relevant for holed tensile members, where geometric stress concentration and interruption of load-oriented filaments coexist and can jointly promote early damage initiation.

The objective of this work is therefore to demonstrate that key load-dependent path-planning concepts, namely deposition-path continuity and alignment with the main load direction, can be transferred to purely polymeric FFF infill through a geometry-driven algorithm. The proposed method locally deviates the infill trajectories around holes while preserving their global alignment with the tensile load direction.

Compared with the current state of the art, the contribution of the present work is fourfold. First, a purely geometric adaptive infill algorithm is introduced, requiring only slicing information and the prescribed load direction. Second, the strategy is implemented in a slicing-compatible workflow that modifies only the infill while leaving perimeters and top/bottom layers unchanged. Third, its mechanical effect is systematically assessed on holed tensile specimens by varying both hole size and hole geometry. Fourth, Digital Image Correlation is used to interpret the resulting strain redistribution and fracture-path modification relative to conventional slicer-generated infills.

Experimental validation focuses on planar specimens with a central hole, which provide a controlled benchmark for isolating the role of path continuity in the vicinity of stress concentrators. The mechanical behaviour obtained with the proposed adaptive infill is compared with that of conventional infills generated by a standard slicer.

2. Materials and methods

2.1. Adaptive infill: Geometrical strategy

The deposition strategy proposed in this work is inspired by the natural organisation of fibres in wood, particularly in the vicinity of knots. In these regions, which are characterised by high stress concentrations, fibres are not interrupted but gradually deviate their paths in order to bypass the defect, thereby preserving the structural continuity of the material. Moreover, the fibre paths extend across the entire component along the load application direction without interruptions, as far as permitted by the geometry, undergoing only local deviations. This biomimetic principle represents an effective model for defining the infill of FFF components containing holes or internal cavities.

In conventional slicing software, the standard aligned rectilinear infill, typically oriented along the main load direction, generates toolpaths that are interrupted whenever a perimeter is encountered, without distinction. Within a single layer, an internal perimeter is geometrically equivalent to a hole of arbitrary shape; consequently, standard infill produces lines that terminate directly at the hole boundary. Since, according to solid mechanics, stress peaks are concentrated precisely along this boundary, the interruption of deposition lines further amplifies the structural criticality.

The proposed strategy instead introduces an adaptive infill, in which deposition lines are locally deviated to follow the component geometry and bypass holes. This approach allows a significantly larger number of deposited lines, interpretable as actual structural fibres, to traverse the component continuously, thereby reducing the number of toolpaths that terminate at the hole surface.

The bypassing of the hole achieved by the adaptive infill, also referred to as tree-style infill, enables the creation of a more extensive network of continuous fibres compared to conventional deposition, improving the component's ability to transfer load without triggering localised weak points. As schematically illustrated in Fig. 1, this biomimetic behaviour produces a material flow that is more consistent with the stress distribution, potentially resulting in an enhanced mechanical response.

The same geometric construction logic may in principle be extended beyond the hole geometries investigated in this work. In particular, local deviation of deposition lines may also be applied to other internal or boundary features, provided that sufficient geometric space is available for path construction. In the present study, however, the experimental validation is intentionally restricted to components with central holes, which offer a controlled benchmark for isolating the effect of path continuity in the vicinity of a stress concentrator.

2.2. Algorithm workflow

The algorithm for generating the deposition toolpaths was developed in Python, chosen both for its widespread adoption and for the availability of numerous open-source libraries that facilitate implementation. In particular, the workflow relies on standard numerical and plotting libraries (NumPy, Matplotlib, math) and a graphical interface toolkit (PyQt5), combined with the FullControl library for toolpath handling and with command-line invocation of the PrusaSlicer engine for the initial slicing stage. The algorithm was integrated into a complete software framework, also developed in Python, which provides an intuitive interface accessible even to non-expert users. This integration allows the application to automatically exploit information derived from previous slicing stages, as well as other user-defined parameters.

The proposed strategy generates only the infill using the adaptive methodology described herein, while all other features (perimeters, top/bottom layers, supports, etc.) are retained as produced by a conventional

Table 1
Positioning of the present work with respect to recent path-planning and discontinuity-aware deposition studies relevant to FFF and material extrusion.

Reference	Process / material system	Main planning principle	Treatment of holes / discontinuities	Main limitation with respect to the present work
Xia et al. [59]	Polymeric FFF	Stress-based tool-path planning	Load-aligned path generation	Requires preliminary stress analysis
Zhang et al. [60]	Polymeric FFF	Partition of principal stress field for toolpath generation	Field-guided path organisation	Requires principal-stress-field evaluation
Kubalak et al. [38]	Material extrusion	Optimized toolpath planning	Orientation/trajectory optimization	Not formulated as a simple geometry-only hole-bypass strategy
Yan et al. [40]	Polymeric FFF	Principal-stress-direction-aware streamlined paths	Feature-aware streamlined path planning	Requires stress-field information
Schiele et al. [61]	FFF	Biomechanical optimization of printing paths	Optimization applied to perforated tensile cases	Optimization-driven rather than slicing-only
Zhang et al. [62]	3D-printed open-hole composites	Fibre placement along the load flow	Explicit open-hole reinforcement	Composite-specific material system
Wang et al. [63]	Continuous fibre reinforced thermoplastic composites	Path planning driven by geometric features and tensile properties	Explicit discontinuity-aware continuous paths	Requires continuous-fibre process and dedicated planning framework
Stelmaszek et al. [64]	Continuous-fibre filament AM	Automated path generation for parts with holes	Explicit hole-aware path generation	Requires continuous-fibre hardware/process
Hou et al. [65]	Curvilinear fibre-reinforced composites	FEA-based curvilinear path design	Hole bypassing through simulation-guided deposition	Composite-based and simulation-driven
Present work	Polymeric FFF	Purely geometric adaptive infill based on slicing information and load direction	Explicit local deviation around holes with global load alignment	No preliminary simulation; compatible with standard slicing/G-code workflows

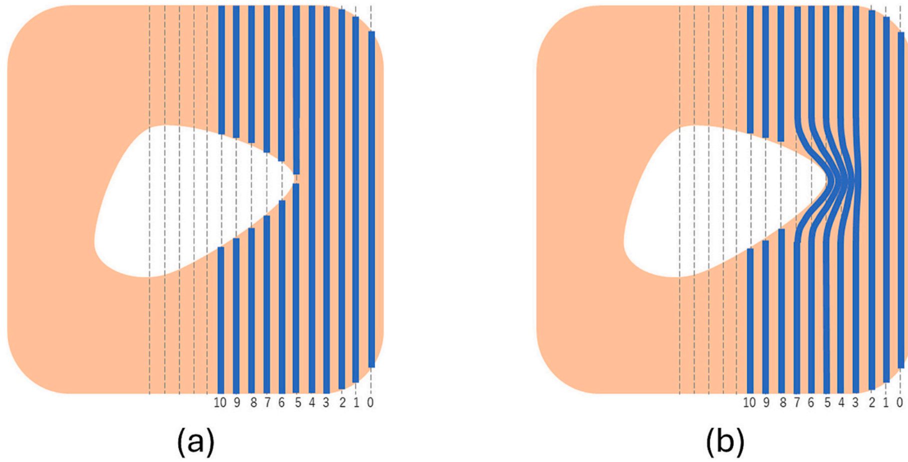

Fig. 1. Comparison between infill strategies: (a) infill line arrangement generated by a conventional slicer using an aligned rectilinear pattern; (b) infill line arrangement generated using the proposed adaptive tree-style infill strategy.

slicing software. The initial slicing stage is therefore performed using a standard slicer, specifically Prusa Slicer [68], which generates a complete G-code file according to the selected parameters. The G-code is then parsed and interpreted to extract the various features and their defining points, with the aim of identifying, for each layer, the regions to be modified.

2.2.1. Step 1 — Infill area extraction

The infill and perimeter points are first read from the G-code. Infill points located far from the perimeter are discarded, retaining only those in proximity to internal surfaces. This procedure enables the identification of the outer rings and inner rings that delimit the infill region to be generated (Fig. 2).

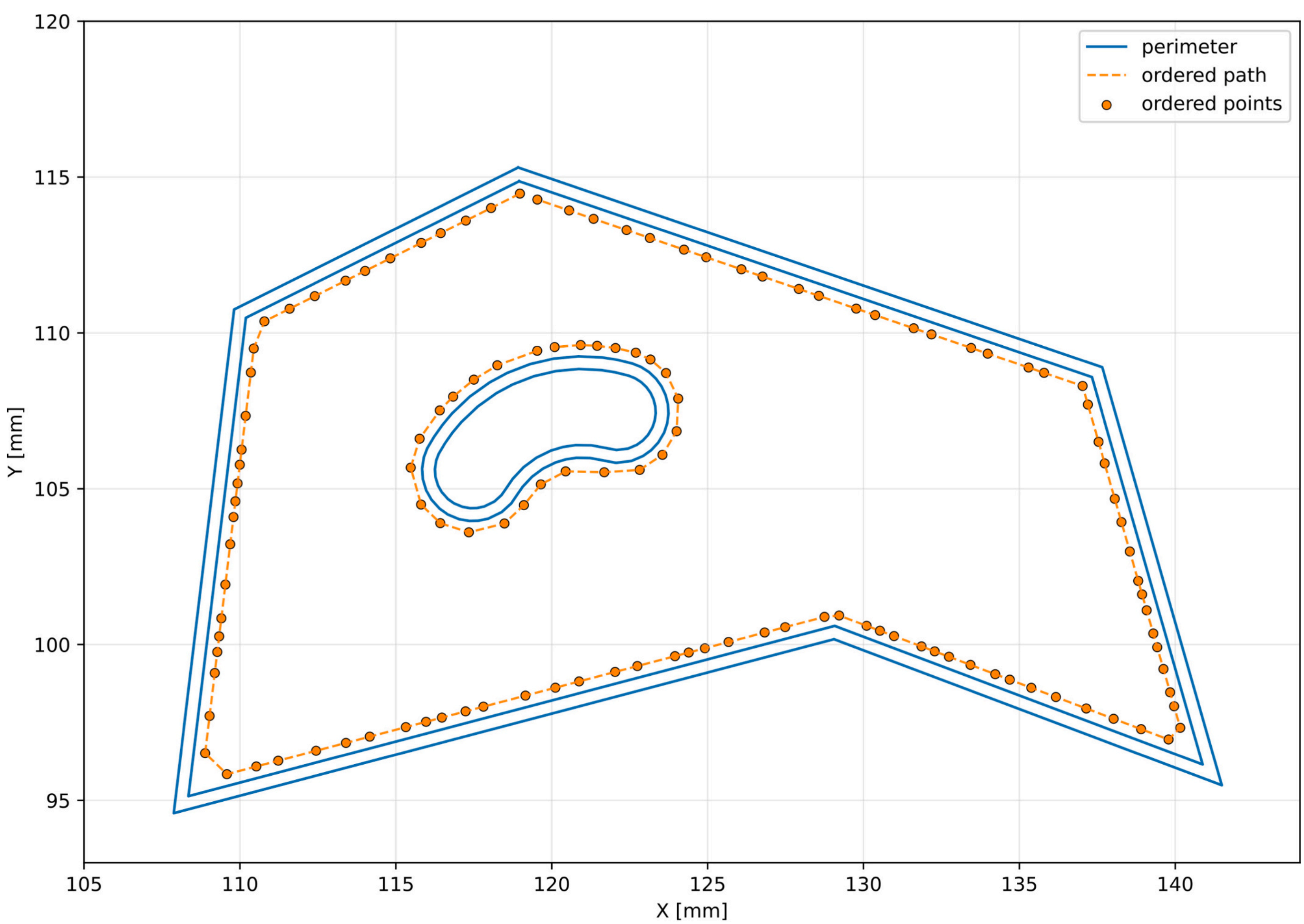

Fig. 2. Plot of one layer in a generic component with a hole. The outer and inner perimeters are shown together with the infill points located in their proximity. These points are subsequently connected to identify closed rings defining the infill domain.

2.2.2. Step 2 — Counting intersections on scanlines

Scanlines are then generated at a constant spacing, where the spacing depends on the infill density as defined by:

$$scanline\ step\ distance = \frac{line\ width}{infill\ density} \tag{1}$$

The scanlines act as construction lines and enable indexed handling of the infill lines throughout all subsequent stages of the algorithm.

For each scanline, the number of intersections with the outer and inner rings is computed. This number is used to classify the scanline behaviour. The classification rules, illustrated in Fig. 3, are as follows:

- 0 intersections: the scanline does not intersect any ring → discarded.
- 1 intersection: degenerate case → treated as the lower even case (0 intersections).
- 2 intersections: the scanline crosses the infill region → points between intersections 1 and 2 are retained.
- 3 intersections: scanline with one crossing and one isolated intersection → treated as the 2-intersection case.
- 4 intersections: the scanline enters and exits the infill region twice → a decision is required on whether to deviate or interrupt the line between intersections 2–3.
- 5 intersections: analogous to the 4-intersection case, with an additional isolated intersection → treated as the 4-intersection case.
- 6 intersections: two complete crossings of the infill region (intersections 1–2, 3–4, 5–6) → deviation will again be evaluated at a later stage.

The process continues analogously for an increasing number of intersections.

2.2.3. Step 3 — Definition of bypass splines

For scanlines exhibiting four intersections (or equivalent cases), the number of lines that can be deviated around the hole is determined dynamically for each layer and for each hole geometry. The criterion is purely geometric and is based on the available space between the outer ring and the inner ring, measured orthogonally to the scanline direction. The minimum distance d_{min} between the two rings defines a local packing constraint: given the prescribed line width and infill density, only a finite number of scanlines can be accommodated without overlap. The cumulative occupied width of non-deviable scanlines is computed as:

$$d_{scan} = n_{scanline} * line\_width \tag{2}$$

and the remaining available distance is then calculated as:

$$d_{available} = d_{min} - d_{scan} \tag{3}$$

represents the maximum admissible region for bypassing. This formulation explicitly limits the local packing density of the deviated lines and prevents material overcrowding in the vicinity of the hole. Scanlines exceeding this geometric constraint are therefore classified as non-deviable and are terminated at the inner ring.

2.2.4. Step 4 — Generation of deviated lines

Among the scanlines identified as deviable, the two closest to the inner ring, one on each side of the hole, are selected first. For these scanlines, a bypass spline is generated between intersections 2 and 3, following the profile of the inner ring, as shown in Fig. 4, in order to ensure continuity of the deposition path. Subsequent scanlines are deviated by applying an outward offset of the inner ring profile with a distance equal to the line width. This construction maintains a constant spacing between adjacent splines and ensures that the local distance between neighbouring deposition paths remains compatible with the nominal extrusion width, preventing material overlap in regions of high curvature. The bypass splines are connected to their respective scanlines through tangential fillets, whose radius is constrained to be greater than or equal to the minimum radius of the innermost spline, ensuring geometric regularity and manufacturability. When local geometric conditions do not allow the generation of a curved fillet, the algorithm automatically introduces a straight connecting segment that preserves path continuity and spacing constraints.

2.2.5. Step 5 — Generation of the remaining infill lines

The remaining lines are divided into two categories:

- Non-deviable lines: scanlines that cannot be deviated and therefore terminate on the inner ring are constructed by drawing segments between intersections 1–2 and 3–4 (drawn in red in Fig. 5a).
- Lines not intersecting the inner ring: these are generated sequentially, from the scanline closest to the inner ring to the farthest, in order to comply with the geometry imposed by the already generated deviated lines (drawn in purple in Fig. 5a).

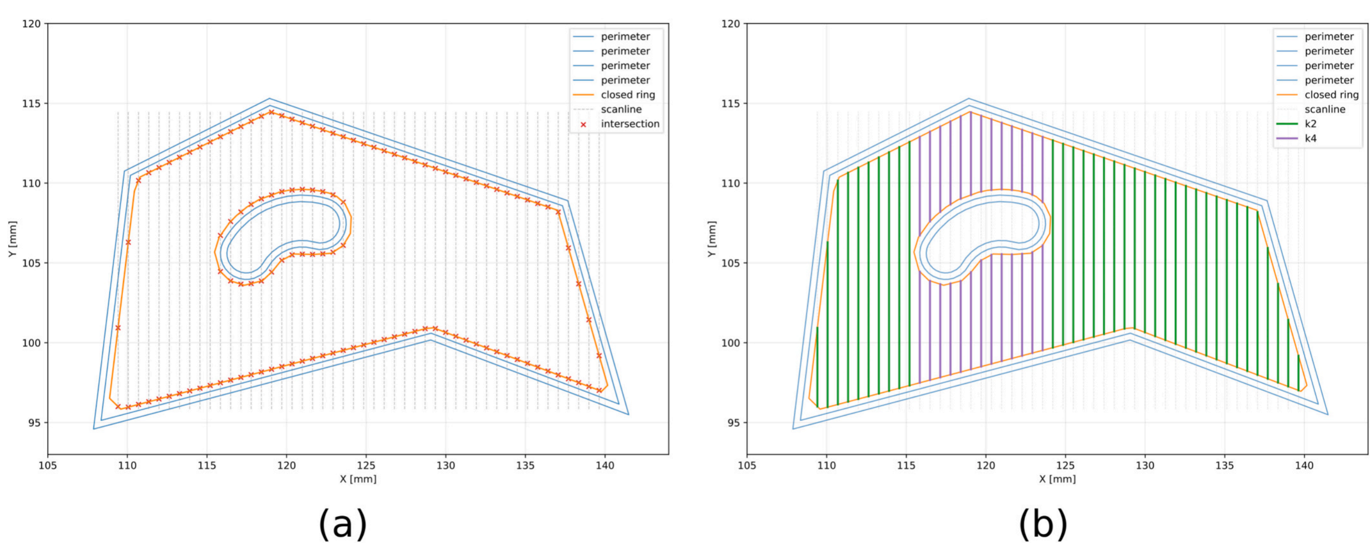

Fig. 3. (a) Plot showing vertically oriented scanlines; cross markers indicate the intersection points between scanlines and inner/outer rings. (b) Classification of scanlines based on the number of intersections with the rings: scanline with 2 intersections (k2 - green), scanline with 4 intersections (k4 - purple). (For interpretation of the references to colour in this figure legend, the reader is referred to the web version of this article.)

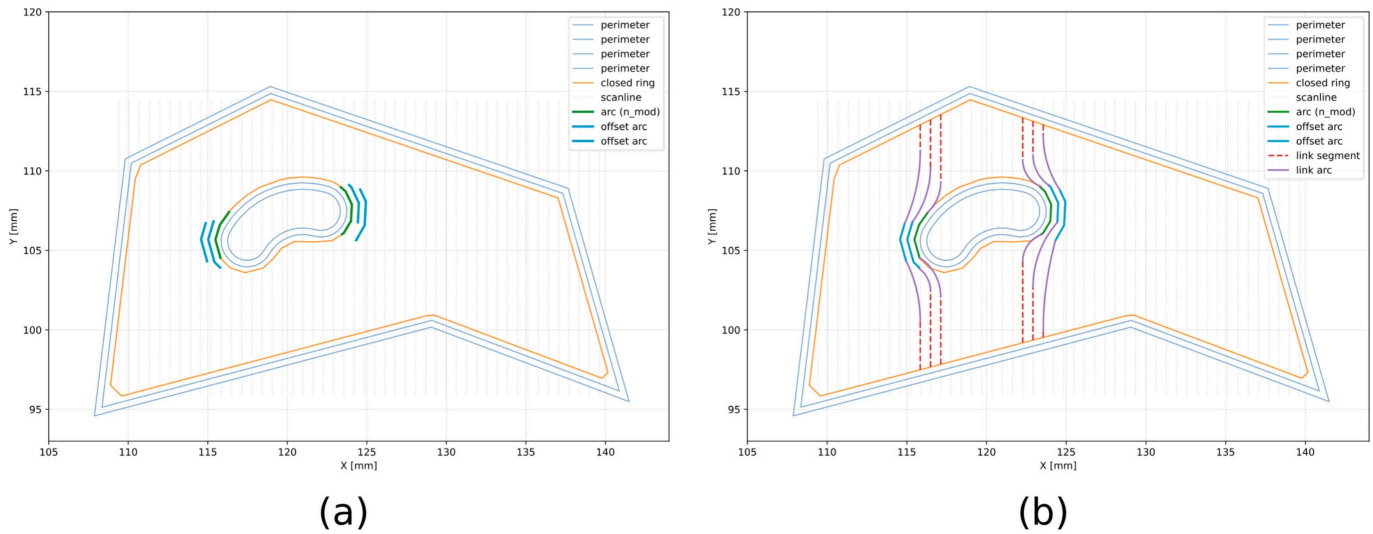

Fig. 4. (a) Generation of the deviation splines (green) and the corresponding offset curves (light blue). (b) Definition of the connections between splines and their reference scanlines through tangential fillets and straight segments. (For interpretation of the references to colour in this figure legend, the reader is referred to the web version of this article.)

An incremental algorithm constructs these lines by following the offset progression while maintaining the spacing within the interval defined by the scanline distance and the line width.

2.2.6. *Step 6 — Generation of the final polyline and G-code*

The toolpaths generated in the previous steps are optimally merged to obtain a single, sequential path that explicitly distinguishes between extrusion segments and travel movements, and is therefore directly suitable for conversion into G-code instructions (Fig. 5b).

The algorithm processes the model on a layer-by-layer basis, starting from the first layer and repeating the same sequence of operations until the final layer is reached. Upon completion, the G-code corresponding to the adaptive infill is seamlessly integrated into the original G-code file containing all other unmodified features, resulting in a final file ready for export and execution on the printing system.

From a computational standpoint, the algorithm operates sequentially on a layer-by-layer and line-by-line basis and is not parallelized in its current implementation. As a consequence, the execution time depends on several factors, including the component geometry, the number and complexity of the internal boundaries, the imposed infill density, the resulting number of generated scanlines, and the computational resources of the adopted hardware. Although the present work does not aim at providing a benchmark study of execution times, this behaviour should be explicitly noted because it directly reflects the geometric construction logic of the method.

At the present stage of development, some geometric configurations may still challenge the robustness of the algorithm. In particular, critical cases include holes or internal boundaries with concave regions, as well as holes located very close to the external perimeter of the component. In such situations, the local space available for deviation may become insufficient or geometrically ambiguous, reducing the reliability of the automatic path construction. These cases do not invalidate the proposed approach, but define the current boundary of applicability of the implementation adopted in this work and indicate a clear direction for future algorithmic refinement.

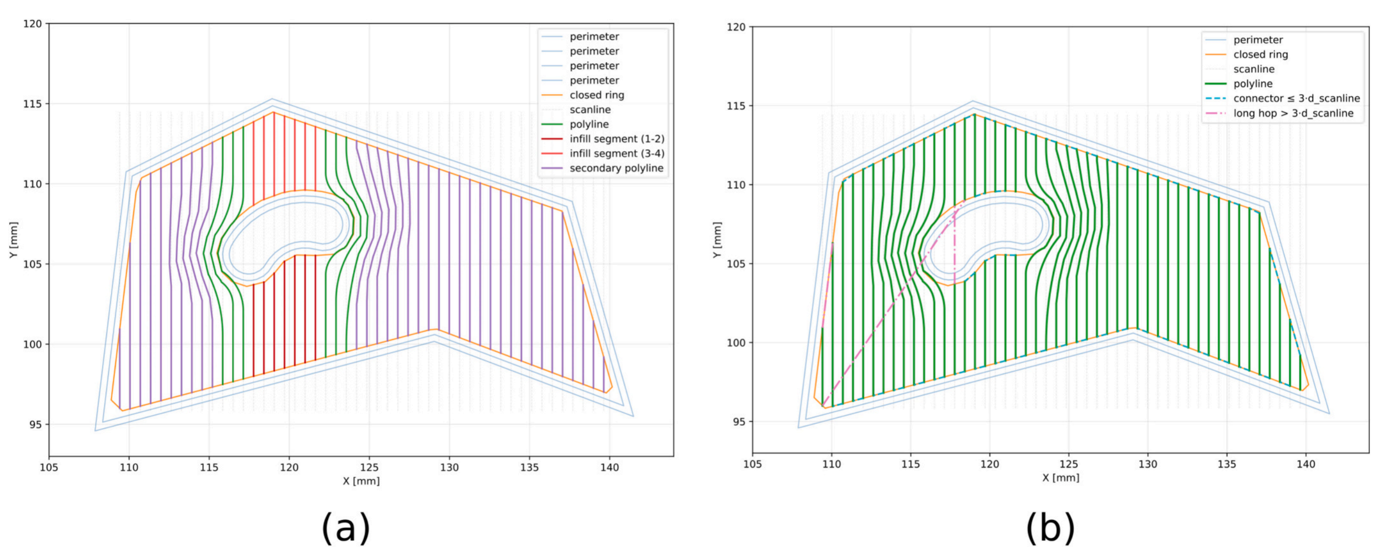

Fig. 5. (a) Identification of non-deviable scanlines (red) and scanlines that do not directly intersect the inner ring but still require deviation (purple). (b) Merging of all infill segments into a single polyline, distinguishing deposition paths (green) from travel moves (pink dashed line). (For interpretation of the references to colour in this figure legend, the reader is referred to the web version of this article.)

2.2.7. Practical implementation on products with complex geometries

Although the experimental validation was intentionally carried out on planar tensile specimens with a single central hole, the proposed workflow is not intrinsically limited to this geometry. Since the method acts at the slicing level, it operates on the two-dimensional contour information available for each layer. A three-dimensional product with a complex shape can therefore be treated as a sequence of layer-wise planar domains, bounded by external perimeters and, when present, by internal boundaries such as holes, slots, cavities, pockets, or other functional features.

This layer-wise formulation is particularly suitable for products containing through-holes or features whose projected contour evolves gradually along the build direction. In these cases, the algorithm adapts the deviated paths from layer to layer because the available space between internal and external boundaries is recalculated independently for each slice. For components with multiple holes, the same logic can be applied to each internal boundary when the corresponding influence regions do not overlap. When holes are close to each other or to the external perimeter, the packing criterion described in Eqs. (2) and (3) acts as a manufacturability check: only the scanlines that can be deviated without violating the prescribed spacing are modified, whereas the remaining lines are generated as non-deviable segments.

For complex industrial parts, the method should therefore be interpreted as a local reinforcement rule rather than as a global replacement of the entire infill. Its most direct application is in regions where the nominal load path is known and internal features interrupt load-aligned filaments. If several load directions are expected during service, the current implementation requires the designer to select the most critical direction or to define different reinforced regions for different load cases. The method does not automatically solve a multi-load-path optimisation problem, nor does it replace finite element analysis when the stress state is unknown.

2.3. Specimen geometry

In order to define the specimen geometry, the relevant standards for the mechanical characterisation of polymeric materials were examined. Since the proposed deposition strategy is specifically designed to optimise components containing at least one hole, the classical dog-bone geometry prescribed by standard testing methods could not be adopted. Such a geometry introduces a necking region between the gripping sections and the gauge section, which would lead to a local variation in deposition strategy, generating an optimized region not directly related to the presence of the hole and thus altering the interpretation of the results.

A rectangular geometry was therefore selected, defined in accordance with the proportions indicated in ISO 527 [69], in which a centrally located hole was introduced. The dimensions were adjusted to ensure specific aspect ratios. The plan view and the adopted dimensions are reported in Fig. 6.

During the experimental campaign, the size and geometry of the hole were varied while all other parameters were kept constant, in order to analyse the evolution of the mechanical behaviour as a function of these variables.

Geometries that would otherwise feature sharp corners were modified by introducing fillets with a radius of 1 mm at such locations, in order to avoid excessive stress concentrations. The load-bearing cross-sectional area was nevertheless maintained constant across the different hole geometries.

2.4. Specimens 3D printing

To validate the developed algorithm, an initial series of printing trials was carried out to verify the correct behaviour of the generated toolpaths. Subsequently, the tensile specimens required for experimental validation of the proposed deposition strategy were fabricated.

All specimens were printed using a Prusa MK3S printer [68] and white Elegoo PLA filament [70]. The printing process was conducted in a controlled environment, maintained at a constant temperature of 25 °C with relative humidity below 30%. Both the filament and the printed specimens were stored under dried conditions prior to testing, in order to prevent variations in material properties due to moisture absorption.

The tensile specimens were oriented vertically on the build plate and centred along the width, as illustrated in Fig. 7a and d. All specimens were fabricated using identical printing parameters, except for the infill density, infill angle, and infill pattern, which were varied as described to investigate their influence on the mechanical behaviour of the specimens.

To compare the proposed adaptive infill with conventional slicer-generated strategies, three standard infill patterns were selected: aligned rectilinear, line, and grid. These patterns were chosen because they are commonly available in conventional slicing software and are

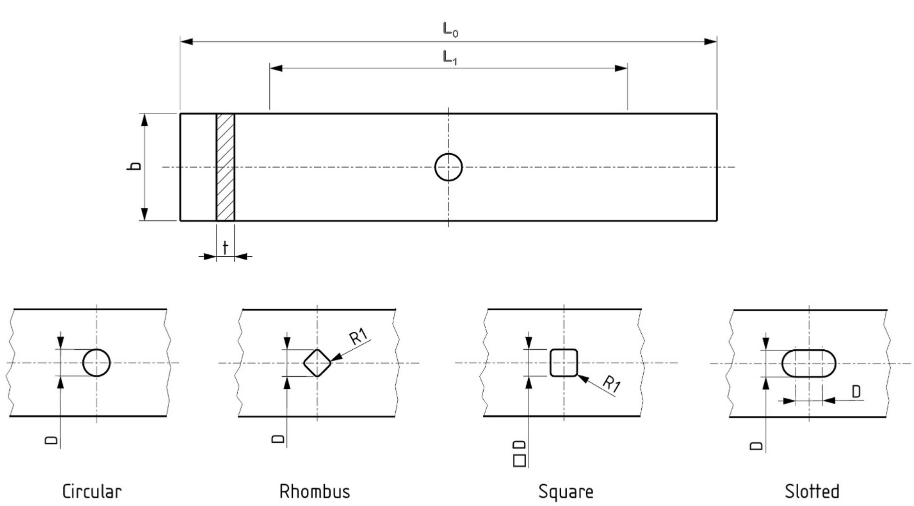

b [mm]	L_0 [mm]	L_1 [mm]	t [mm]	D [mm]
30	150	100	5	6 / 7.5 / 10

Fig. 6. Dimensioned geometry of the tensile specimen and hole configurations, positioned at the specimen mid-width depending on the hole type. The holes have a diameter D, varied in this study over three values: 6, 7.5, and 10 mm.

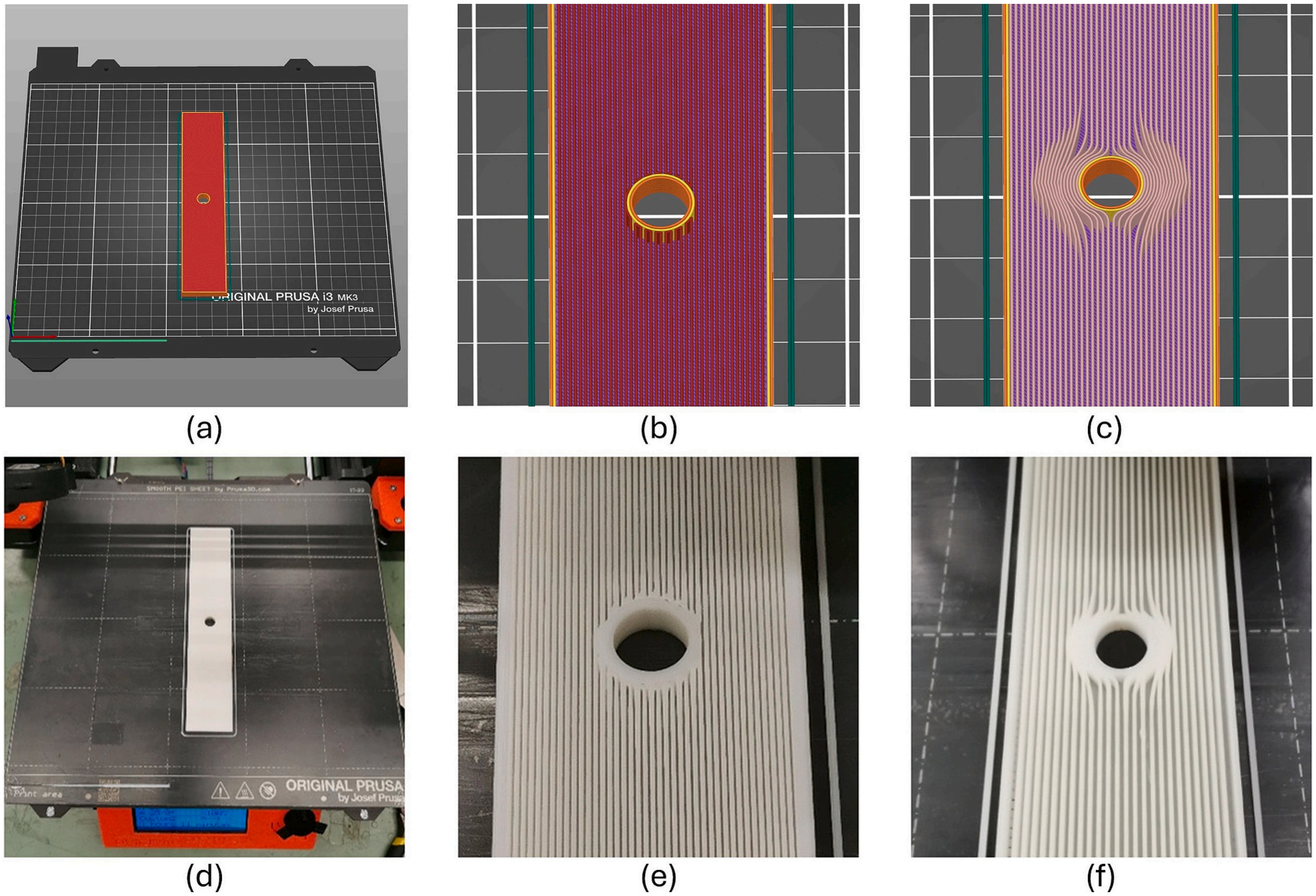

Fig. 7. Tensile specimen with a 7.5 mm central circular hole and 60% infill density fabricated using a Prusa MK3S printer. The completed print and its placement on the build plate are shown in the slicer view (a) and on the printer (d). The printing sequence of the aligned rectilinear P1 specimen is shown in the slicer (b) and on the printer (e), while that of the adaptive A5 specimen is shown in the slicer (c) and on the printer (f).

among the most mechanically relevant configurations reported in the literature for FFF components.

For ease of identification throughout fabrication, testing, and data analysis, each specimen configuration was assigned an alphanumeric code. The complete list of specimen types and their main characteristics is reported in Table 2.

Parameters not directly involved in the analysis were set in accordance with values commonly adopted in the literature. In particular, four top layers and four bottom layers were used, as the absence of these layers may introduce anomalous behaviour under load. The number of perimeters was fixed at two, in order to prevent them from becoming the dominant load-bearing feature while still providing the necessary structural contribution. The line width was set to 0.45 mm for all features (infill, perimeters, and top/bottom layers), ensuring uniformity in deposition and filament dimensions. The main printing parameters are summarised in Table 3.

Table 2
List of specimen configurations and main characteristics.

Name	Hole shape	Infill type	Infill angle [°]	Infill density [%]	Aspect ratio	D [mm]
A1	Circular	Adaptive	0	40	3	10
A2	Circular	Adaptive	0	80	3	10
A3	Circular	Adaptive	0	60	3	10
A4	Circular	Adaptive	0	40	4	7.5
A5	Circular	Adaptive	0	60	4	7.5
A6	Circular	Adaptive	0	80	4	7.5
A7	Circular	Adaptive	0	40	5	6
A8	Circular	Adaptive	0	60	5	6
A9	Circular	Adaptive	0	80	5	6
P1	Circular	Aligned rectilinear	0	60	4	7.5
P2	Circular	Line	45	60	4	7.5
P3	Circular	Grid	45	60	4	7.5
B1	Rhombus	Adaptive	0	60	4	7.5
B2	Rhombus	Aligned rectilinear	0	60	4	7.5
C1	Square	Adaptive	0	60	4	7.5
C2	Square	Aligned rectilinear	0	60	4	7.5
D1	Slotted hole	Adaptive	0	60	4	7.5
D2	Slotted hole	Aligned rectilinear	0	60	4	7.5

2.5. Experimental test

To validate the proposed deposition strategy, tensile tests were performed to evaluate the mechanical behaviour of the printed specimens. For each specimen, the principal geometric dimensions relevant to characterisation were measured, namely the specimen width, the thickness at the hole section, and the diameter (or width) of the hole along the load-bearing section. All geometric quantities and the derived stress-based parameters reported in this work were calculated using these measured dimensions rather than the nominal CAD values. In addition, all specimens were weighed to quantify deviations from the

Table 3
Printing parameters used for all tested specimens.

Parameters	Value	Unit
First layer height	0.2	mm
Layer height	0.2	mm
Extrusion width	0.45	mm
Infill anchor	2.5	mm
Infill anchor max	12	mm
Infill angle	0–45 [1]	°
Infill density	40–60–80	%
Infill overlap	10	%
Skirt distance	2	mm
Skirt height	3	layers
Skirts	2	–
Brim type	No	–
Bottom fill pattern	Monotonic	–
Bottom solid layers	4	–
Top fill pattern	Monotonic	–
Top solid layers	4	–
Perimeters	2	–
Perimeter generator	Classic	–
First layer speed	20	mm/s
External perimeter speed	25	mm/s
Perimeter speed	45	mm/s
Top solid infill speed	40	mm/s
Infill speed	80	mm/s
Solid infill speed	80	mm/s
Arc fitting	No	–
Elephant foot compensation	0	mm
Bed temperature	60	°C
First layer bed temperature	65	°C
First layer temperature	215	°C
Printing temperature	210	°C
Nozzle diameter	0.4	mm
Min fan speed	50	%
Max fan speed	100	%
Disable fan first layers	1	layers
Full fan speed layer	4	layer

[1] The infill angle depends on the pattern used, as reported in Table 2: 0° for adaptive and aligned rectilinear infill, and 45° for line and grid infill.

mass estimated by the slicer and to enable weight-normalised performance evaluation. Measurements were carried out using a digital calliper with a resolution of 0.01 mm and a balance with a resolution of 0.01 g.

Tensile tests were conducted using a Shimadzu AGX-V2 [71] universal testing machine with a 100 kN capacity, equipped with a Shimadzu SLFL-100 kN load cell and data acquisition via TrapeziumX-V software. During testing, displacement and applied force were recorded, from which engineering stress and strain values were subsequently derived.

All tests were performed at a constant crosshead speed of 1 mm/min, with a sampling frequency of 100 Hz. Each specimen was clamped at both ends over a length of 25 mm per side, as illustrated in Fig. 8.

To ensure the consistency and repeatability of the experimental results, five identical specimens were tested for each geometric and deposition variant. This allowed the variability of the data to be assessed and the experimental uncertainties associated with the measurements to be quantified.

The calculation of the parameters used in the proposed method is defined by the following expressions:

$$aspect\ ratio = \frac{b_{mean}}{D_{mean}} \tag{4}$$

$$\sigma = \frac{F}{A} \qquad where \qquad A = (b_{mean} - D_{mean}) \bullet t_{mean} \tag{5}$$

$$\varepsilon_{eng} = \frac{\Delta u}{L_1} \tag{6}$$

$$\rho_{app} = \frac{m}{V_{spec,mean}} \tag{7}$$

$$S\rho = \frac{UTS}{\rho_{app}} \tag{8}$$

$$CV = \frac{Standard\ Deviation}{Mean} \bullet 100 \tag{9}$$

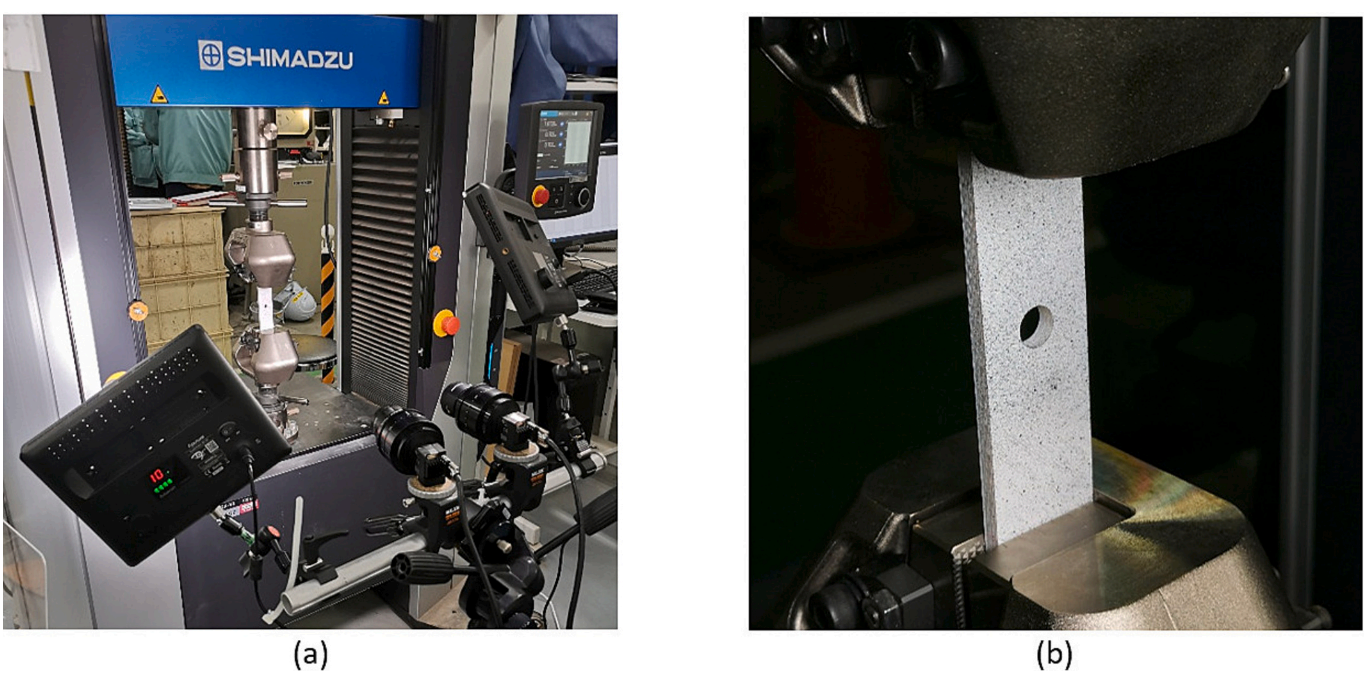

Fig. 8. (a) Experimental setup prior to tensile testing: the specimen is clamped in the grips, the VIC-3D system is properly positioned, and the scene is uniformly illuminated; (b) detail of the specimen surface showing the applied stochastic speckle pattern for DIC analysis.

In the above expressions, b_{mean}, t_{mean}, and D_{mean} denote the measured specimen width, the measured thickness at the hole section, and the measured hole dimension along the load-bearing transverse section, respectively. For non-circular holes, D_{mean} represents the transverse hole dimension measured along the section used to define the net load-bearing area. Δu denotes the crosshead displacement recorded during the tensile test, and the corresponding engineering strain therefore represents a global response referred to the initial gauge length L_1, corresponding to the free specimen length between the grips. The apparent density ρ_{app} used for performance normalisation was calculated from the measured specimen mass m and the corresponding specimen geometric volume $V_{spec,mean}$, consistently accounting for the actual tested geometry. The quantity Sρ reported in the following section therefore represents a strength-to-density ratio, i.e. a specific-strength indicator used to compare configurations on a weight-normalised basis.

The coefficient of variation was calculated to assess the repeatability of the measurements as indicated in eq. 9. Pairwise comparisons between adaptive and corresponding aligned rectilinear configurations were performed using Welch's two-sample *t*-test, with a significance level of α = 0.05, which does not assume equal variances between groups. The test statistic was calculated as:

$$t = \frac{\bar{x} - \bar{x}}{\sqrt{\frac{s_1^2}{n_1} + \frac{s_2^2}{n_2}}} \tag{10}$$

where $\bar{x}$and $\bar{x}$are the sample means, $s_1$and $s_2$are the sample standard deviations, and n_1 and $n_2$are the numbers of specimens in the two groups.

To evaluate the material behaviour beyond the peak stress, the deformation of the region surrounding the hole and the crack formation in the printed specimens were analysed. Given the adopted geometry, the maximum stress level is localised along the hole boundary; consequently, crack initiation inevitably occurs in this region, while crack propagation is influenced by the internal structure defined by the deposition strategy.

The analysis of deformation and fracture evolution was carried out using three-dimensional Digital Image Correlation (3D DIC) with the VIC-3D system (Correlated Solutions) [72]. A dual high-resolution camera setup was employed, appropriately positioned and calibrated to capture the deformation field in the central region of the specimen, in the vicinity of the hole.

To ensure accurate acquisition by the VIC-3D system, a speckle pattern was applied to the specimen surface in two stages: application of a uniform layer of matt white paint; spraying of high-contrast black paint to generate a random distribution of fine speckles. This pattern enables the DIC system to uniquely identify the monitored surface regions, allowing precise evaluation of the localisation, magnitude, and evolution of deformations throughout the entire tensile test.

Image acquisition during the tensile tests was performed at a rate of 1 frame per second. Calibration of the stereo setup was carried out using the calibration targets supplied with the VIC-3D system. Among the strain components available from the DIC post-processing, the ε_{yy} component was selected for the present study, as it is aligned with the tensile loading direction and was found to provide the most informative representation of strain localisation and fracture evolution in the analysed specimens. Unless otherwise stated, the contour maps discussed later in Section 3.5 and reported in Fig. 12 refer to the frame corresponding to the maximum UTS of each specimen.

After tensile testing, representative fracture regions were inspected using a Keyence VHX-7100 optical digital microscope equipped with ring-light illumination. The observations were used to compare fracture traces, secondary cracks, and damage distribution between adaptive and aligned rectilinear infill specimens, complementing the DIC-based failure analysis discussed in Section 3.5.

The experimental investigation initially focused on comparing the developed adaptive infill with selected conventional infill patterns, and subsequently on analysing the component behaviour as a function of specific geometric and process parameters. The main results obtained from the tensile tests are summarised in Table 4.

3. Results

3.1. Comparison between adaptive infill and conventional infill patterns

The proposed adaptive infill was compared with the principal infill patterns available in conventional slicing software, selected on the basis of their mechanical performance as reported in the literature. In particular, Aligned Rectilinear, Line, and Grid infills were considered, hereafter referred to as P1, P2, and P3, respectively. Based on the experimental results, and as shown in Fig. 9, the conventional infill exhibiting the best performance is the Aligned Rectilinear pattern, whose behaviour most closely approaches that of the adaptive infill.

A comparison of the main parameters derived from the tensile tests highlights that the adaptive infill leads to a systematic improvement across all the analysed quantities. Specifically, increases are observed in ultimate tensile strength (UTS), elastic modulus, engineering strain, and absorbed energy with respect to conventional infill patterns.

When comparing the adaptive infill with the Aligned Rectilinear pattern, which represents the best compromise among the analysed standard infills, an increase in ultimate tensile strength of 18% is observed, accompanied by a slight increase in both elastic modulus (+4%) and engineering strain at maximum load (+19%). As shown in Fig. 9, in addition to the higher peak value, the adaptive infill exhibits a significantly larger area under the stress–strain curve than conventional infills, indicating a superior energy absorption capability prior to fracture.

3.2. Influence of aspect ratio and infill density

The specimens were divided into two main categories. The first category focused on specimens with a circular hole, investigating the influence of hole size, expressed in terms of aspect ratio, and infill density. The second category examined the effect of hole geometry while keeping both infill density and aspect ratio constant.

To evaluate the combined influence of aspect ratio and infill density, three different aspect ratios and three infill density levels were considered; the corresponding results are summarised in Fig. 10. As shown in Fig. 10a, at a fixed aspect ratio, increasing the infill density leads to an approximately linear increase in ultimate tensile strength. Conversely,

Table 4
Tensile test results for the tested specimen types.

Name	UTS [1] [MPa]	Strain at UTS [1] [%]	Elastic Modulus [MPa]	Specific strength [kJ/kg]
A1	30.48 ± 0.309	2.54 ± 0.063	1887.69 ± 79.2	38.53 ± 0.52
A2	38.40 ± 0.893	2.53 ± 0.064	2354.15 ± 151.2	35.39 ± 0.84
A3	35.46 ± 0.372	2.60 ± 0.029	2125.36 ± 194.0	37.71 ± 0.44
A4	29.37 ± 0.363	2.74 ± 0.102	1709.18 ± 20.4	36.83 ± 0.49
A5	37.40 ± 0.324	2.92 ± 0.083	2046.68 ± 5.5	38.28 ± 0.38
A6	40.84 ± 0.828	2.84 ± 0.034	2474.90 ± 232.1	36.51 ± 0.79
A7	30.24 ± 0.294	2.96 ± 0.049	1899.97 ± 3.8	38.25 ± 0.55
A8	36.52 ± 0.651	3.17 ± 0.049	1915.01 ± 72.2	37.28 ± 0.74
A9	42.22 ± 0.486	3.09 ± 0.021	2612.91 ± 41.8	38.00 ± 0.58
P1	31.71 ± 0.428	2.45 ± 0.015	1982.26 ± 34.9	33.51 ± 0.47
P2	23.15 ± 0.374	2.81 ± 0.465	1424.15 ± 44.3	24.17 ± 0.39
P3	22.60 ± 0.199	2.36 ± 0.037	1604.46 ± 20.0	23.36 ± 0.23
B1	37.50 ± 0.162	2.77 ± 0.016	2364.72 ± 9.5	39.52 ± 0.34
B2	32.35 ± 0.065	2.24 ± 0.036	2310.81 ± 15.7	34.41 ± 0.19
C1	37.14 ± 0.103	2.81 ± 0.042	2326.51 ± 8.3	38.47 ± 0.17
C2	33.03 ± 0.164	2.25 ± 0.023	2303.10 ± 6.6	34.76 ± 0.36
D1	38.24 ± 0.348	2.77 ± 0.025	2370.22 ± 8.6	39.73 ± 0.38
D2	31.87 ± 0.133	2.04 ± 0.049	2301.63 ± 1.3	34.13 ± 0.20

[1] Ultimate Tensile Strength.

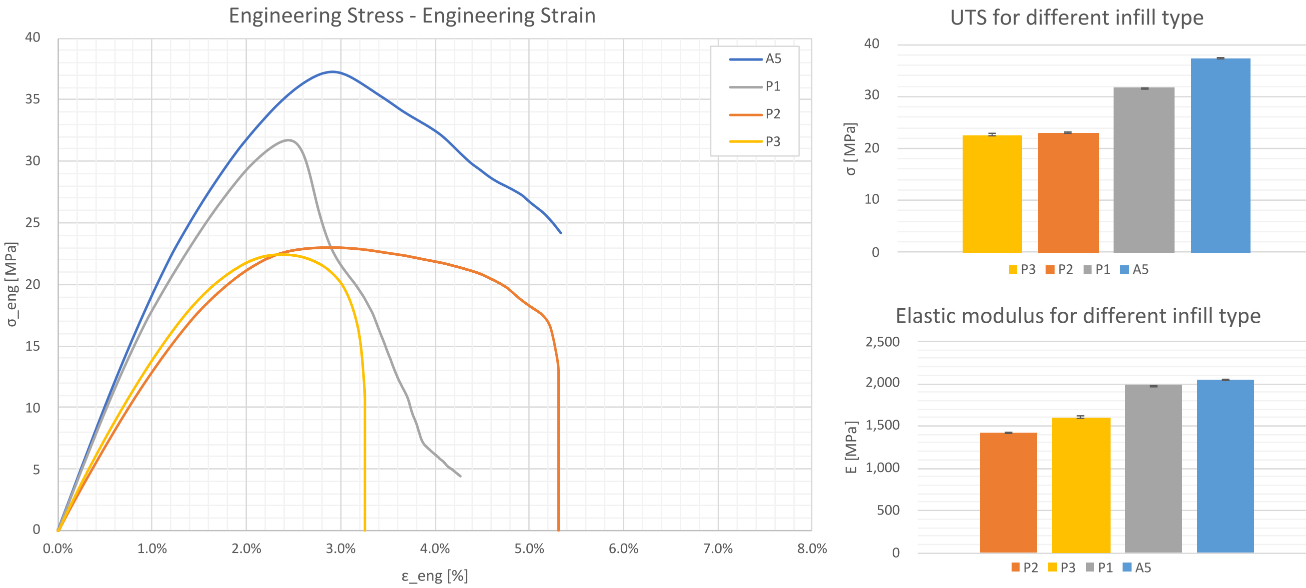

Fig. 9. Comparison of the mechanical response of specimens with a circular central hole of D = 7.5 mm, aspect ratio = 4, and infill density = 60%. The adaptive infill design A5 is compared with conventional infill patterns P1, P2, and P3, corresponding to aligned rectilinear, line, and grid infill, respectively. The figure reports the stress-engineering strain curves together with the corresponding ultimate tensile strength (UTS) and elastic modulus values.

at a fixed density, variation of the aspect ratio results in a differentiated behaviour: for infill densities of 40% and 60%, no significant variation in ultimate tensile strength is observed, whereas at an infill density of 80% a slight increase is recorded with increasing aspect ratio. This behaviour can be attributed to the fact that an infill density approaching full solid yields a mechanical response closer to that of an ideal homogeneous plate, for which the aspect ratio becomes an influential parameter.

Fig. 10b shows that, at a fixed aspect ratio, the engineering strain remains approximately constant, whereas at a fixed infill density the strain increases with increasing aspect ratio. Finally, Fig. 10c indicates that the elastic modulus increases with increasing aspect ratio.

In order to compare specimens characterised by different infill densities on a weight-normalised basis, the specific strength Sρ, defined as the ratio between ultimate tensile strength and apparent specimen density, was used as an additional performance indicator. As specified in Section 2.5, the apparent density was calculated from the measured specimen mass and the corresponding specimen geometry. This parameter, reported in Table 4, enables identification of the most efficient infill configuration, i.e. the one providing the greatest mechanical benefit at equal weight. The most effective configurations are A1, A5, A7, and A9, with values exceeding 38 kJ/kg, whereas the least effective configurations are A2 and A6. All specimens with conventional infill exhibit values 20–40% lower than those of the best-performing adaptive configurations.

3.3. *Influence of holes*

To investigate the influence of hole geometry on the mechanical behaviour of the specimens, the experimental tests were carried out while keeping the aspect ratio fixed at 4 and the infill density at 60%, thereby isolating the effect of hole geometry alone on the obtained results.

Although the holes exhibit different geometries, the width measured along the load-bearing transverse section of the specimen was maintained constant for all configurations, ensuring an equivalent load-bearing cross-section. As described in Section 2.3, the analysed geometries include circular, square, rhomboidal, and slot-shaped holes.

Comparison of the UTS values for the four geometries shows that the adaptive infill consistently leads to a significant improvement in

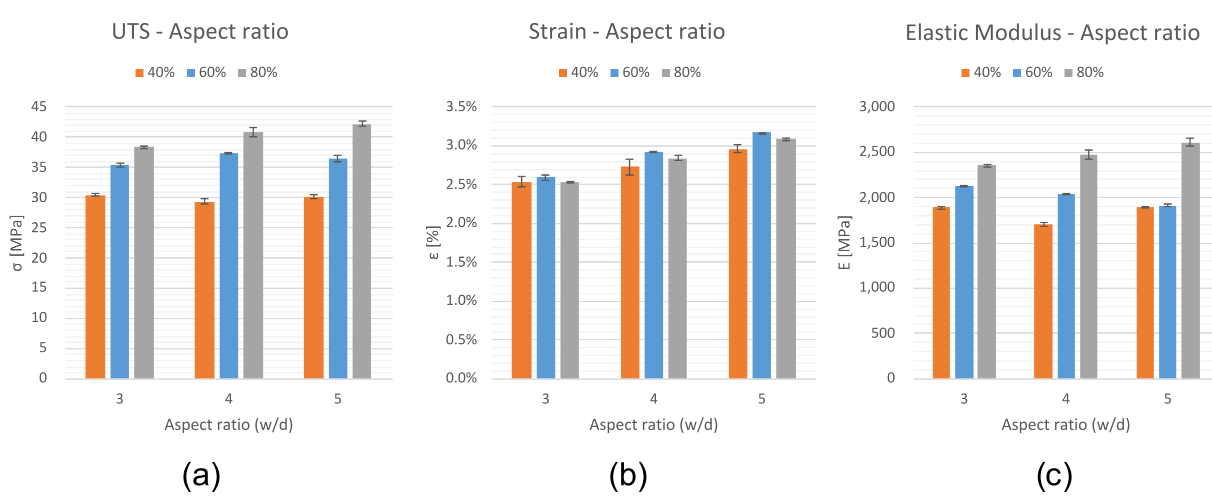

Fig. 10. Bar charts illustrating the behaviour of specimens with a circular hole and adaptive infill as a function of aspect ratio and infill density. The plots report the main mechanical properties analysed: (a) Ultimate Tensile Strength (UTS), (b) strain at UTS, and (c) elastic modulus.

performance with respect to the conventional infill generated by the slicer. In particular, an increase in ultimate strength ranging from 12% to 20% is observed: the minimum improvement occurs for the square hole (from 33.04 MPa to 37.12 MPa), whereas the maximum increase is recorded for the slot-shaped hole (from 31.88 MPa to 38.23 MPa). This improvement is systematic and independent of hole shape, confirming the robustness of the proposed strategy across the non-circular hole geometries analysed in this study, as shown in Fig. 11.

Analysis of the engineering strain at maximum load reveals an increase of 19% for the circular hole, while the square and rhomboidal holes exhibit increases of 23% and 25%, respectively. The slot-shaped configuration shows a markedly higher deformation compared to the other geometries, with a strain increase of 35%.

The elastic modulus exhibits a slight increase (up to 3%) for specimens with circular and slot-shaped holes. For the rhomboidal hole, the increase is reduced to 2.3%, while no appreciable variation is observed for the square hole. These results indicate that hole geometry has a limited influence on the global stiffness of the component, while exerting a more pronounced effect on strength and deformability-related parameters.

3.4. Statistical analysis

A statistical analysis was performed to assess the repeatability of the experimental data and to support the comparison between the adaptive and conventional infill configurations. The coefficient of variation (CV) was calculated for the main mechanical properties reported in Table 4, namely UTS, strain at UTS, elastic modulus, and specific strength. The corresponding values are reported in Table 5.

Overall, the CV values indicate good repeatability of the experimental results. For UTS, the CV remains below 2.5% for all configurations, while the CV of specific strength is also consistently low, remaining below 2.4%. The strain at UTS shows limited scatter in most cases, with the only notable exception of specimen P2, for which a higher variability is observed. The elastic modulus exhibits larger variability for some adaptive configurations, especially A3 and A6; however, the overall trends remain consistent with the mechanical results discussed in the previous sections.

To evaluate whether the differences between adaptive and aligned rectilinear infill were statistically significant, pairwise comparisons were performed using Welch's two-sample t-test. The analysis was performed for each hole geometry by comparing specimens with the same hole shape, aspect ratio, and infill density, differing only in the infill strategy. The corresponding two-tailed p-values are reported in Table 6.

The statistical analysis confirms that the adaptive infill produces statistically significant differences with respect to the aligned rectilinear infill for all investigated hole geometries and for all analysed properties ($p < 0.05$). The strongest statistical evidence is observed for UTS, strain at UTS, and specific strength, supporting the effectiveness of the proposed strategy in improving the load-bearing capacity and deformation

Table 5
Coefficient of variation of the experimental results.

Name	UTS CV [%]	Strain at UTS CV [%]	Elastic modulus CV [%]	Specific strength CV [%]
A1	1.01	2.48	4.20	1.35
A2	2.33	2.53	6.42	2.37
A3	1.05	1.12	9.13	1.17
A4	1.24	3.72	1.19	1.33
A5	0.87	2.84	0.27	0.99
A6	2.03	1.20	9.38	2.16
A7	0.97	1.66	0.20	1.44
A8	1.78	1.55	3.77	1.98
A9	1.15	0.68	1.60	1.53
P1	1.35	0.61	1.76	1.40
P2	1.62	16.55	3.11	1.61
P3	0.88	1.57	1.25	0.98
B1	0.43	0.58	0.40	0.86
B2	0.20	1.61	0.68	0.55
C1	0.28	1.49	0.36	0.44
C2	0.50	1.02	0.29	1.04
D1	0.91	0.90	0.36	0.96
D2	0.42	2.40	0.06	0.59

Table 6
Welch's two-sample t-test comparison between adaptive and aligned rectilinear infill.

Comparison	Hole shape	UTS p-value	Strain at UTS p-value	Elastic modulus p-value	Specific strength p-value
A5 vs P1	Circular	2.74E-08	1.60E-04	1.37E-02	1.75E-07
B1 vs B2	Rhombus	7.11E-09	2.46E-07	4.06E-04	5.90E-08
C1 vs C2	Square	9.38E-10	1.40E-07	1.32E-03	1.34E-06
D1 vs D2	Slotted hole	1.63E-07	1.08E-07	4.38E-05	9.56E-08

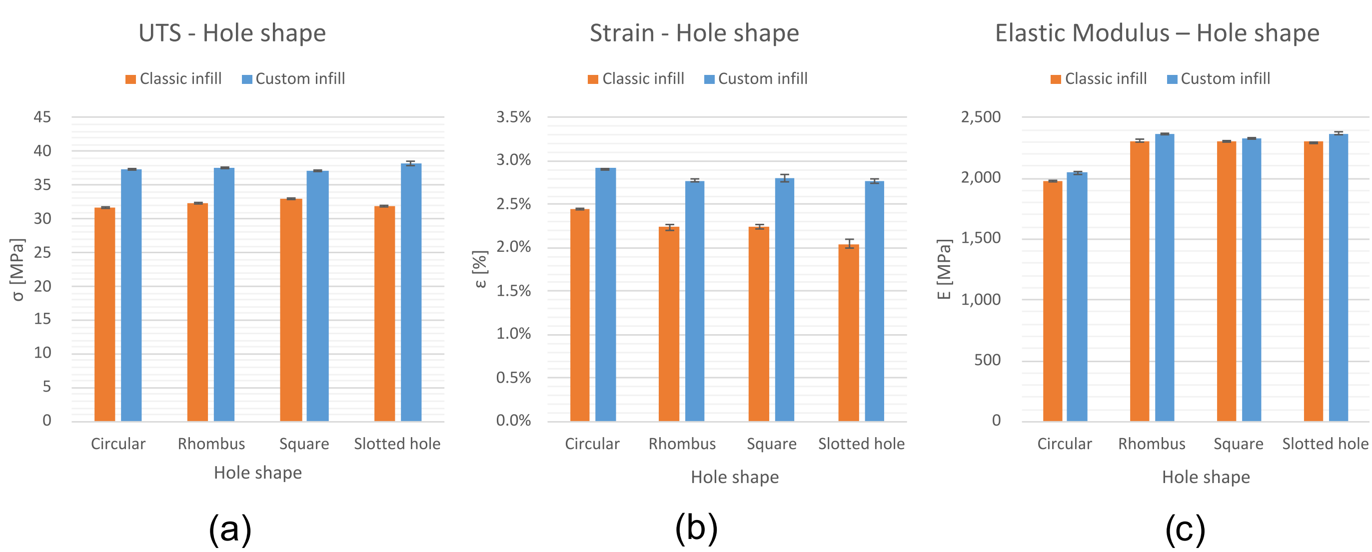

Fig. 11. Bar charts illustrating the behaviour of specimens with constant aspect ratio equal to 4 and constant infill density of 60% as a function of hole geometry. The plots report: (a) ultimate tensile strength (UTS), (b) strain at UTS, and (c) elastic modulus.

capability of the specimens.

Although statistically significant differences are also observed for the elastic modulus, the relative increase in stiffness remains moderate compared with the improvements in UTS, strain at UTS, and specific strength. This suggests that the adaptive infill does not primarily act by producing a global stiffening effect. Rather, its main contribution is associated with the modification of damage initiation and crack propagation mechanisms, as further discussed through the DIC and fracture analyses.

3.5. Digital image correlation and fracture analysis

To gain deeper insight into the infill behaviour under load, Digital Image Correlation (DIC) was employed to evaluate the strain distribution on the specimen surface during tensile testing. In the present study, the εyy strain component was analysed, as it is aligned with the tensile loading direction and provides the clearest representation of strain localisation in the region surrounding the hole. Unless otherwise specified, the strain contour maps discussed in this section and shown in Fig. 12 correspond to the frame associated with the maximum UTS of each specimen. This analysis complements and corroborates the observations derived from the global mechanical results discussed in the previous sections.

Specimens manufactured with conventional infill exhibit a behaviour consistent with solid mechanics theory for a holed plate subjected to tensile loading. Strain initially localises along the inner edge of the hole, at the minimum load-bearing section, as illustrated in Fig. 12a. In this region, the primary crack initiates and subsequently propagates predominantly in the horizontal direction until reaching the external perimeter of the component, which represents the last region capable of sustaining load prior to final failure.

In contrast, specimens manufactured with adaptive infill display a markedly different behaviour, directly attributable to the different organisation of the internal structure. As in the conventional case, the maximum stress concentration remains localised near the hole, as indicated by the high measured εyy strain and the initiation of an initial crack in this region. However, as the tensile test proceeds, this crack does not evolve into a stable propagation path. Instead, further load increase induces the formation of new cracks at the external perimeter of the component, not aligned with the minimum load-bearing section, which propagate from the outside towards the hole and ultimately lead to specimen failure. It is noteworthy that cracks originating at the external perimeter never connect with the initial crack formed at the hole boundary.

This behaviour confirms that the region surrounding the hole remains subject to the highest stress concentration, as predicted by theory, also considering that the perimeters are identical in specimens with conventional and adaptive infill, thus ensuring a consistent experimental comparison. Unlike conventional infill, however, the crack does not find a preferential propagation path originating from the hole, as the deviated infill lines that bypass the hole generate a locally reinforced region capable of hindering fracture advancement. Conversely, the external region of the

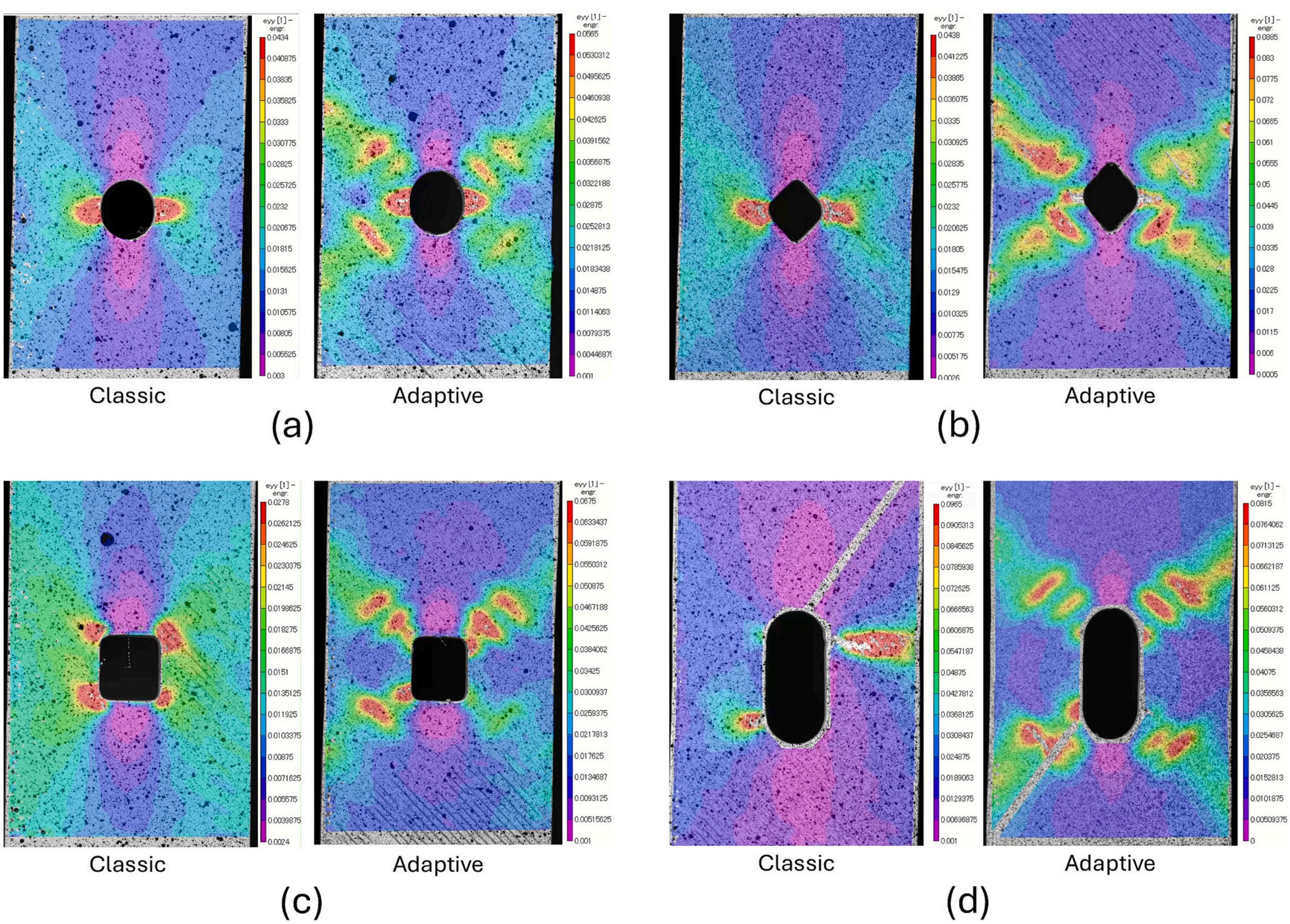

Fig. 12. Comparison of εyy strain contour maps obtained by DIC at the UTS frame for specimens with: (a) circular, A5 and P1; (b) rhomboidal, B1 and B2; (c) square, C1 and C2; and (d) slot-shaped hole, D1 and D2. In each pair, the aligned rectilinear configuration is shown on the left and the adaptive configuration on the right.

component, where the arrangement of deposition lines is similar to that of conventional infill, remains more susceptible to the initiation of new cracks.

This altered mechanism of crack initiation and propagation was consistently observed for all analysed hole geometries, confirming the effectiveness of the adaptive infill strategy in modifying fracture paths

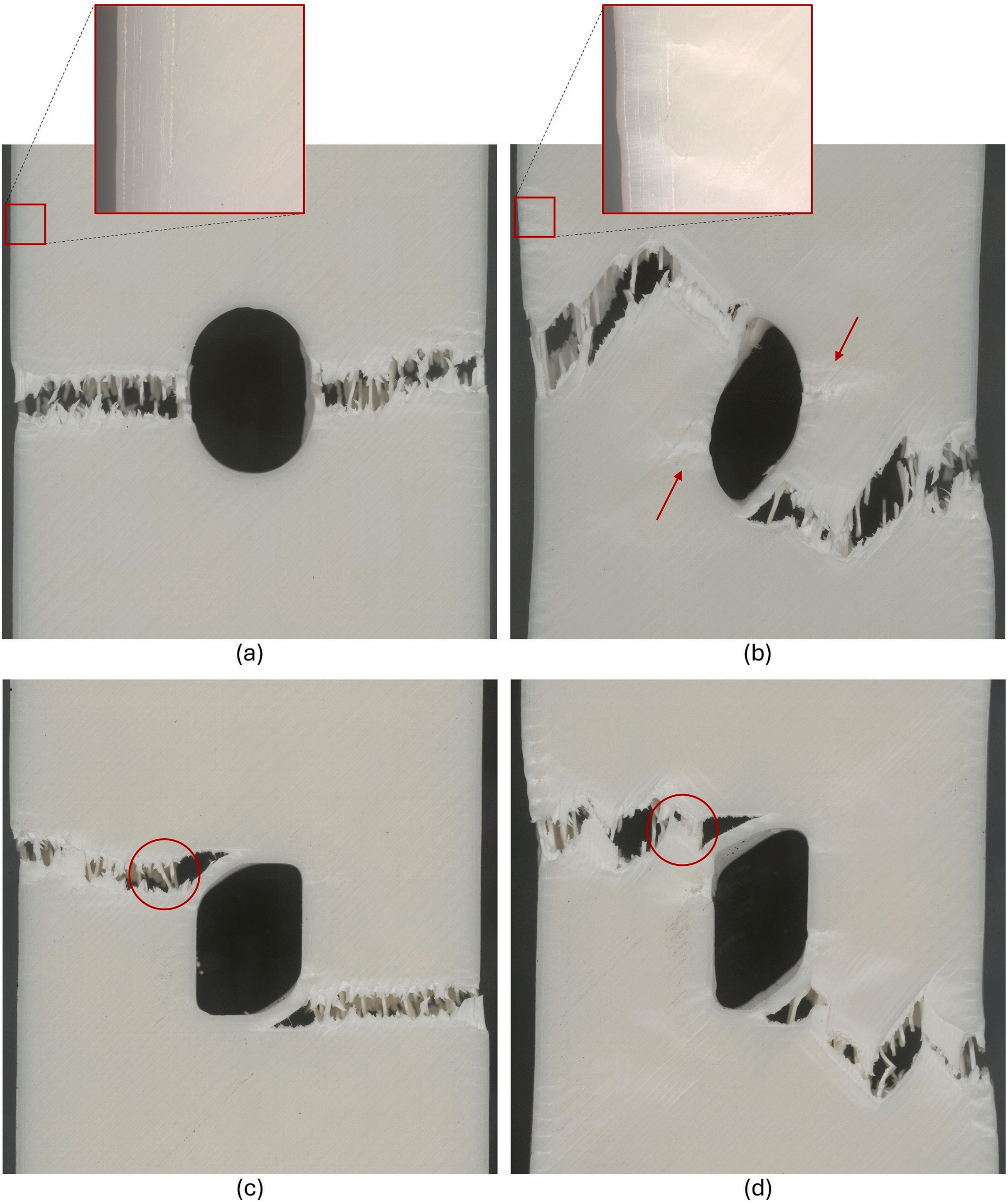

Fig. 13. Optical microscopy analysis of the fracture surfaces of the specimens: (a) P1, (b) A5, (c) C2, and (d) C1.

and enhancing the overall strength of the component.

An additional aspect emerging from the DIC analysis concerns the evolution of hole deformation during testing. Near the onset of crack initiation, deformation induces a tendency for hole closure, attributable to the fact that the infill lines bypassing the hole tend to straighten under load. This effect is more pronounced for larger holes and for the slot-shaped geometry, whereas square and rhomboidal holes exhibit a stiffer response.

In the case of conventional infill, the strain distribution follows the analytical solution, with concentration at the hole extremities aligned with the minimum load-bearing section, as visible in Fig. 12. For circular and rhomboidal geometries, fracture initiates along the minimum section and propagates outward towards the external perimeter. For square and slot-shaped geometries (Fig. 12c and d), in which a single minimum section cannot be clearly identified and a broader critical region exists instead, fracture initiates within this region at locations corresponding to opposing curvature changes. This behaviour is particularly evident for the slot-shaped geometry, where fracture develops on the upper right and lower left sides.

In contrast, specimens with adaptive infill exhibit a recurring cross-shaped surface strain distribution centred on the hole, with principal directions inclined by approximately 45° with respect to the specimen axis. This behaviour is attributable to the fact that, in these regions, the infill lines undergo the greatest deviation from the load application direction. As a result, strain is distributed over a wider area and is less localised exclusively at the hole, a condition that contributes to the experimentally observed increase in ultimate failure load.

The optical inspection of the fracture regions provides further evidence supporting the failure mechanisms identified by DIC. Fig. 13 compares specimens A5 and P1, both with a circular hole of 7.5 mm and 60% infill density, manufactured with adaptive and aligned rectilinear infill, respectively. In both specimens, fracture traces are visible along the external perimeter and tend to coalesce into a preferential crack path after reaching the infill/top-layer region.

The main difference concerns the extent of damage around the hole. In P1, secondary cracks are mainly localised close to the main fracture path. In A5, a larger number of secondary cracks and damage traces is distributed over a wider region around the hole. This indicates that a larger material volume participates in load transfer before final failure, consistently with the broader strain redistribution observed by DIC. Although several cracks initiate from the internal and external perimeters, only a limited number of them propagate through the whole specimen and lead to rupture.

The fracture path of A5 does not simply follow the minimum resistant section. Local damage still initiates near this region, but final crack propagation occurs along less reinforced paths above and below the hole and is additionally influenced by the top-layer deposition direction. This confirms that the adaptive infill does not suppress the stress concentration at the hole boundary, but modifies crack propagation by preserving local infill continuity around the discontinuity.

Similar fracture features were observed for the other hole sizes and geometries. The square-hole specimens shown in Fig. 13c and d further highlight the role of the adaptive path arrangement. In C1, the deviated infill lines pass close to the hole corner and contribute to opposing crack initiation from this critical region, whereas in C2 the aligned rectilinear infill is interrupted at the internal perimeter. Since the square hole produces a stronger notch effect than the circular hole, its geometry still significantly affects the mechanical response. Nevertheless, the adaptive infill also improves the ultimate strength in this configuration, confirming that local path continuity can mitigate the detrimental effect of geometric stress concentration.

4. Discussion

The experimental results indicate that the proposed adaptive infill improves the mechanical response of holed FFF specimens primarily by modifying the local organisation of the load-bearing filaments rather than by producing a simple global stiffening effect. This is evident from the fact that the most consistent gains are observed in ultimate tensile strength, strain at maximum load, and absorbed energy, whereas the increase in elastic modulus remains comparatively limited. In the comparison with conventional slicer-generated patterns, the aligned rectilinear infill represents the most competitive baseline, yet the adaptive strategy still provides higher tensile strength and larger deformation at the maximum load. This behaviour suggests that the principal effect of the proposed strategy is not a uniform increase in specimen rigidity, but rather a more efficient redistribution of deformation in the vicinity of the stress concentrator.

This interpretation is consistent with recent mechanically informed toolpath studies. Kubalak et al. [38] showed that optimized toolpath planning in material extrusion can improve part performance by aligning deposition with a prescribed orientation field, while Sadeghieh et al. [39] reported strength gains through stress-oriented trajectory planning in FFF. Although those approaches rely on orientation fields or stress-based planning, the present results follow the same general trend: the largest benefits arise when deposition orientation and path continuity are treated as structural variables rather than as purely geometric filling choices. The fact that the present gains are more pronounced in UTS and strain at maximum load than in elastic modulus is also coherent with the observations of Allum et al. [1], who showed that alternative toolpaths may primarily act by redirecting the fracture path and delaying failure rather than by producing a proportional increase in small-strain stiffness.

A second relevant outcome concerns the role of geometry and density. For circular holes, increasing infill density leads to the expected increase in strength, whereas the influence of aspect ratio remains limited within the explored range for densities up to 60%. Only at 80% infill density does aspect ratio begin to exert a more appreciable effect, which is consistent with the fact that the printed structure progressively approaches the behaviour of a more homogeneous solid. In addition, the analysis of strength normalised with respect to density indicates that several adaptive configurations outperform the conventional ones even when mass efficiency is considered. This confirms that the mechanical benefit is not achieved through a simple increase in deposited material, but through a more effective geometric organisation of the infill.

The comparatively limited influence of aspect ratio for densities up to 60% is worth comparing with previous studies on conventionally printed open-hole polymer plates. Khosravani and Reinicke [50] reported a clearer dependence of tensile performance on the width-to-hole-diameter ratio in standard FDM plates, where the net-section geometry directly governs the structural response. A plausible explanation for the milder aspect-ratio sensitivity observed here is that the adaptive infill partly compensates for the geometric severity of the hole by preserving a larger number of continuous load-oriented paths in its vicinity. The residual aspect-ratio effect observed at 80% infill is nevertheless consistent with the open-hole literature, since as the internal architecture becomes denser the specimen progressively approaches the behaviour of a more continuum-like plate, for which net-section geometry regains greater importance.

The statistical analysis supports the robustness of these trends. The generally low coefficients of variation indicate good repeatability, while Welch's t-test confirms that the differences between adaptive and aligned rectilinear infill are significant for all investigated hole geometries. This is relevant because the analysed holes differ in curvature, local ligament shape, and strain-concentration behaviour, yet the adaptive strategy remains beneficial in all cases.

The magnitude of the improvement nevertheless depends on geometry. The largest UTS increase is obtained for the slotted hole, where the conventional infill produces an extended region of filament interruption and the adaptive bypass can preserve continuity over a wider critical area. Conversely, the square hole shows a smaller, although still significant, improvement, likely because abrupt curvature changes reduce the space available for smooth path deviation. Finally, the specific-strength results confirm that the benefit is not merely due to increased mass or density, but to a more efficient organisation of the deposited material.

The DIC observations provide a mechanistic interpretation of these trends. In specimens with conventional infill, strain localisation and crack initiation occur at the hole boundary and evolve along a preferential path associated with the minimum resistant section. In contrast, in specimens with adaptive infill, the first crack still nucleates near the hole, as expected from the geometric stress concentration, but does not develop into a stable propagation path. Instead, the deviated lines surrounding the hole act as a locally reinforced zone that hinders crack advance and promotes damage development in external regions of the specimen. The recurring cross-shaped strain pattern observed around the hole in the adaptive configurations is consistent with the local deviation of the infill lines from the tensile axis and with the redistribution of strain over a wider area. From a structural standpoint, the adaptive strategy therefore preserves the geometric stress concentration, but reduces the extent to which this concentration is amplified by the interruption of load-oriented filaments at the hole boundary.

This fracture-based interpretation is also aligned with related observations in the literature. In ZigZagZ non-planar printing, Allum et al. [1] associated improved strength, strain-at-fracture, and toughness with a redirection of the fracture path and an increased tendency towards through-filament failure. Likewise, Krajangsawasdi et al. [55] showed in open-hole tensile tests on aligned discontinuous composites that steering the raster around the hole changes the failure mode relative to conventionally cut-hole specimens. The present DIC evidence supports an analogous mechanism in polymer-only FFF: the adaptive path does not suppress the geometric stress concentration itself, but changes the way in which localised deformation evolves into a propagating crack.

When interpreted in the context of the literature, these results support the central hypothesis of the work: concepts commonly associated with load-dependent path planning can be transferred to polymer-only FFF infill without relying on preliminary finite element simulations or on continuous-fibre hardware. In this sense, the present strategy differs from stress-field-driven or optimisation-based approaches, in which path generation depends on principal-stress evaluation, streamline construction, or dedicated composite-oriented deposition frameworks. The contribution of the present work is therefore not to maximize the absolute mechanical performance attainable with advanced composite systems, but to demonstrate that a significant fraction of the same design logic, namely continuity of the deposition path around holes while preserving global load alignment, can be implemented through a purely geometric and slicing-compatible workflow. This point is particularly relevant for routine FFF applications, where ease of integration, robustness, and low computational overhead are often more important than the maximum achievable performance.

This difference in scope also helps explain why the gains reported here are more moderate than those observed in continuous-fibre or strength-optimized composite studies [55,57]. In those cases, the benefits derive not only from path steering, but also from substantially higher reinforcement efficiency, stronger anisotropy along the fibre direction, and, in some cases, concurrent topology and fibre-path optimization. By contrast, the present study intentionally isolates the contribution of geometry-driven path continuity in an unreinforced polymer FFF workflow. The fact that measurable improvements are still obtained under these more constrained conditions is therefore an important result in itself.

From an application perspective, the proposed strategy offers a favourable trade-off between mechanical improvement and implementation simplicity. The algorithm modifies only the infill, while keeping perimeters, top/bottom layers, and the rest of the slicing workflow unchanged. This makes the method compatible with standard FFF practice and suitable for implementation either directly in the slicer or as a post-processing step on the G-code, as done in the present work. At the same time, the scope of the present validation should be clearly acknowledged. The experimental campaign is limited to tensile loading of planar specimens with a central hole, fabricated in a single polymeric material and on a single printing platform. Moreover, although the observed trends are systematic, the present study is not intended as a full statistical characterisation of the process. Future work should therefore extend the validation to additional loading conditions, different materials, more complex discontinuities, and quantitative comparisons with simulation-driven path-planning methods. Within these boundaries, the results nevertheless demonstrate that local continuity of load-aligned deposition paths is an effective design variable for improving the mechanical performance of FFF components containing central holes.

4.1. Advantages and limitations of the proposed adaptive infill strategy

The proposed adaptive filling method presents several practical advantages. It improves the tensile performance of holed FFF specimens without increasing nominal infill density or material usage, because the gain is obtained by reorganising the existing infill paths around the internal discontinuity. The method is also purely geometry-driven: it requires only the sliced geometry and the prescribed load direction, without preliminary finite element analysis, principal-stress extraction, or iterative optimisation. Moreover, only the infill is modified, while perimeters, top and bottom layers, supports, and the remaining slicer-generated features are preserved. This makes the strategy compatible with conventional G-code post-processing and suitable for local reinforcement of mechanically critical regions. The DIC results further suggest that the adaptive paths improve damage tolerance by hindering direct crack propagation from the hole boundary.

It is also useful to distinguish the proposed strategy from slicer-based local modifier approaches, available in commercial slicing software. These tools can locally increase infill density and/or add internal walls around selected regions, thereby reinforcing critical areas. However, this reinforcement is mainly achieved by locally increasing the amount of deposited material or by adding wall contributions. In contrast, the present method aims to isolate the effect of infill path continuity around holes while keeping the nominal infill density, number of perimeters, and global material usage comparable between configurations. A direct comparison with slicer-based local modifier strategies would therefore require a dedicated mass-normalised study including different local densities, modifier geometries, wall-count settings, part weight, print time, and setup/processing time.

The method also has limitations. First, a relevant load direction must be known in advance. The current implementation is therefore most suitable for components mainly subjected to a dominant tensile load, whereas multiaxial loading, bending, torsion, impact, fatigue, or multiple competing load cases require the designer to identify the most critical direction or to define different reinforced regions. Second, the method is constrained by geometry. Smooth path deviation requires sufficient space between internal and external boundaries and between neighbouring holes. Very small ligaments, closely spaced holes, sharp concave regions, or highly irregular contours may prevent the generation of manufacturable bypass paths, requiring the algorithm to reduce the number of deviated lines or locally revert to conventional infill. Third, the algorithm controls the nominal deposition path but does not directly model bead deformation, thermal history, inter-road bonding, or local extrusion stability, which may depend on printer calibration, material rheology, and process parameters.

Finally, the present validation is limited to planar PLA specimens with central holes subjected to quasi-static tensile loading and manufactured on a single FFF platform. The results demonstrate the effectiveness of the proposed concept under controlled conditions; however, they do not yet constitute a complete design database covering different materials, printing systems, loading modes, environmental conditions, or long-term behaviour. Future work should therefore extend the experimental validation to flexural, fatigue, and impact loading, additional materials, and more complex part geometries. A dedicated finite element analysis will also be required in future work to quantify the stress redistribution produced by the adaptive infill and to account for the actual deposited architecture, toolpath arrangement, and process-related features. Such numerical investigation was not included in the present study because the objective was to experimentally isolate the effect of geometry-driven path continuity without relying on preliminary simulations. Within these limits, the method represents a practical strategy for improving the mechanical response of FFF components containing load-critical discontinuities.

5. Conclusion

In this work, a geometry-driven adaptive infill strategy for polymeric FFF components with central holes was developed and experimentally validated. The method preserves the global alignment of the deposition paths with the main load direction while locally deviating them around the hole, treating the infill as a network of virtual structural fibres.

Compared with conventional slicer-generated infills, and in particular with aligned rectilinear infill as the most competitive baseline, the proposed strategy systematically improved the tensile response of the analysed specimens. Ultimate tensile strength increased by 12–20%, strain at maximum load by 19–35%, and absorbed energy also increased, whereas elastic modulus changed only moderately. These results indicate that the main benefit of the method is not a simple global stiffening effect, but a more efficient redistribution of deformation in the vicinity of the stress concentrator.

DIC analysis showed that the adaptive infill changes the fracture mechanism. In conventional infills, cracking initiates at the hole boundary and propagates along a preferential path associated with the minimum resistant section. In the adaptive configurations, the deviated paths create a locally reinforced region around the hole that hinders stable crack propagation from this zone and promotes a broader strain redistribution.

Overall, the present study demonstrates that hole-aware, load-aligned path continuity can improve the mechanical performance of polymer-only FFF components through a purely geometric and slicing-compatible workflow, without preliminary numerical simulations or additional material usage. The method is particularly attractive for practical implementation because it can be applied locally around mechanically critical discontinuities while preserving the conventional slicer-generated perimeters, top and bottom layers, supports, and non-critical infill regions.

Within the limits of the present validation: planar tensile specimens with central holes, one material, one printing platform, and quasi-static tensile loading; the proposed strategy represents a practical route for strengthening holed FFF components. Its application to real products will require geometric feasibility checks, appropriate selection of the dominant load direction, and further validation under more complex loading and manufacturing conditions. These aspects define the main direction for future work, together with the extension of the algorithm to multiple discontinuities, more complex three-dimensional geometries, and quantitative comparison with simulation-driven toolpath-planning methods.

CRediT authorship contribution statement

Andrea Montalti: Writing – review & editing, Writing – original draft, Validation, Software, Methodology, Investigation, Formal analysis, Data curation, Conceptualization. **Taichi Yamashita:** Software, Investigation, Data curation. **Taiyo Nakamura:** Software, Investigation, Data curation. **Alfredo Liverani:** Supervision, Funding acquisition. **Akihiro Takezawa:** Writing – review & editing, Writing – original draft, Visualization, Supervision, Project administration, Methodology, Funding acquisition.

Funding

This research did not receive any specific grant from funding agencies in the public, commercial, or not-for-profit sectors.

Declaration of competing interest

The authors declare that they have no known competing financial interests or personal relationships that could have appeared to influence the work reported in this paper.

References

[1] Allum J, Kitzinger J, Li Y, Silberschmidt VV, Gleadall A. ZigZagZ: improving mechanical performance in extrusion additive manufacturing by nonplanar toolpaths. Addit Manuf 2021;38:101715. https://doi.org/10.1016/j.addma.2020.101715.
[2] Sabik A, Rucka M, Andrzejewska A, Wojtczak E. Tensile failure study of 3D printed PLA using DIC technique and FEM analysis. Mech Mater 2022;175:104506. https://doi.org/10.1016/j.mechmat.2022.104506.
[3] Xiao X, Roh B-M, Zhu F. Strength enhancement in fused filament fabrication via the isotropy toolpath. Appl Sci 2021;11:6100. https://doi.org/10.3390/app11136100.
[4] Guessasma S, Nouri H, Belhabib S. Digital image correlation and finite element computation to reveal mechanical anisotropy in 3D printing of polymers. Materials 2022;15:8382. https://doi.org/10.3390/ma15238382.
[5] Raut NP, Bhosale SM, Salunkhe MS, Kolekar AB, Gombi SL. Effects of part orientation, infill pattern, and infill density on the mechanical properties of 3D printed parts. Mater Today Proc 2021;47:598–603. https://doi.org/10.1016/j.matpr.2021.02.630.
[6] Demir S. Optimization of mechanical properties in FDM 3D-printed PLA parts: evaluating the interaction of key parameters. J Mater Eng Perform 2025. https://doi.org/10.1007/s11665-025-11320-4.
[7] Vieweger D, Diel S, Schweiger H-G, Tetzlaff U. Mechanical properties of raw filaments and printed specimens: effects of Fiber reinforcements and process parameters. Polymers (Basel) 2024;16:1576. https://doi.org/10.3390/polym16111576.
[8] Croccolo D, De Agostinis M, Olmi G. Experimental characterization and analytical modelling of the mechanical behaviour of fused deposition processed parts made of ABS-M30. Mater Des 2013;52:1–8. https://doi.org/10.1016/j.matdes.2013.05.058.
[9] Ayatollahi MR, Nabavi-Kivi A, Bahrami B, Yazid Yahya M, Khosravani MR. The influence of in-plane raster angle on tensile and fracture strengths of 3D-printed PLA specimens. Eng Fract Mech 2020;237:107225. https://doi.org/10.1016/j.engfracmech.2020.107225.
[10] Menargues S, Navas J, Espinosa I, Baile MT, Vaz RF, Picas JA. Effect of additive manufacturing parameters on PLA, ABS, and PETG strength. Processes 2025:13. https://doi.org/10.3390/pr13092733.
[11] Murugan V, Alaimo G, Marconi S, Berke PZ, Massart TJ, Auricchio F. Filament path optimization of fused filament fabricated parts incorporating the effect of pre-fusion densities. Int J Solids Struct 2022;254–255:111916. https://doi.org/10.1016/j.ijsolstr.2022.111916.
[12] Ramos LLB, Iwasaki KMK, Beck R, Scheffer WC, Fuga FR, De Medeiros R. Influence of layer orientation on the mechanical properties of fused deposition modelling using PLA and PETG. Materialia (Oxf) 2025;44:102541. https://doi.org/10.1016/j.mtla.2025.102541.
[13] Jadali A, Abedini V, Kami A. Influence of raster angle and post-processing via hot pressing on the mechanical performance of fused filament fabricated Polylactic acid (PLA) components. Int J Interact Des Manuf (IJIDeM) 2026;20:1233–51. https://doi.org/10.1007/s12008-025-02463-8.
[14] Panico A, Corvi A, Collini L, others. Multi objective optimization of FDM 3D printing parameters set via design of experiments and machine learning algorithms. Sci Rep 2025;15:16753. doi:https://doi.org/10.1038/s41598-025-01016-z.
[15] Rasheed A, Hussain M, Ullah S, Ahmad Z, Kakakhail H, Riaz AA, et al. Experimental investigation and Taguchi optimization of FDM process parameters for the enhancement of tensile properties of Bi-layered printed PLA-ABS. Mater Res Express 2023:10. https://doi.org/10.1088/2053-1591/acf1e7.
[16] Samykano M, Selvamani SK, Kadirgama K, others. Mechanical property of FDM printed ABS: influence of printing parameters. Int J Adv Manuf Technol 2019;102:2779–96. doi:https://doi.org/10.1007/s00170-019-03313-0.
[17] Samykano M. Mechanical property and prediction model for FDM-3D printed Polylactic acid (PLA). Arab J Sci Eng 2021;46:7875–92. https://doi.org/10.1007/s13369-021-05617-4.
[18] Rodr\'\iguez-Panes A, Claver J, Camacho AM. The influence of manufacturing parameters on the mechanical behaviour of PLA and ABS pieces manufactured by FDM: a comparative analysis. Materials 2018.
[19] Çiçek UI, Johnson AA. Multi-objective optimization of FDM process parameters for 3D-printed polycarbonate using Taguchi-based gray relational analysis. Int J Adv Manuf Technol 2025;137:3709–25. https://doi.org/10.1007/s00170-025-15392-3.
[20] Mencarelli M, Sisella M, Puggelli L, Innocenti B, Volpe Y. Sensitivity analysis of 3D printing parameters on mechanical properties of fused deposition modeling printed

Polylactic acid parts. Applied Mechanics 2025;6:17. https://doi.org/10.3390/applmech6010017.
[21] Bouzaglou O, Golan O, Lachman N. Process design and parameters interaction in material extrusion 3D printing: a review. Polymers (Basel) 2023;15:2280. https://doi.org/10.3390/polym15102280.
[22] Aktepe E, Ergün U. Machine learning approaches for FDM-based 3D printing: a literature review. Appl Sci 2025;15:10001. https://doi.org/10.3390/app151810001.
[23] Faizaan M, Shenoy Baloor S, Nunna S, others. A study on the overall variance and void architecture on MEX-PLA tensile properties through printing parameter optimisation. Sci Rep 2025;15:3103. doi:https://doi.org/10.1038/s41598-025-87348-2.
[24] Saberton M. 3D printing bead configuration. 2022.
[25] Sajjad R, Butt SU, Saeed HA, Anwar MT, Rasheed T. Impact of multiple infill strategy on the structural strength of single build FDM printed parts. J Manuf Process 2023;89:105–10. https://doi.org/10.1016/j.jmapro.2023.01.065.
[26] Gupta P, Krishnamoorthy B, Dreifus G. Continuous toolpath planning in a graphical framework for sparse infill additive manufacturing. Comput Aided Des 2020;127:102880. https://doi.org/10.1016/j.cad.2020.102880.
[27] Singh S, Singh A, Kapil S, Das M. Generation of continuous and sparse space filling toolpath with tailored density for additive manufacturing of biomimetics. Comput Aided Des 2024;173:103718. https://doi.org/10.1016/j.cad.2024.103718.
[28] Liu J, Su Z, Wang C, Xu Z. Effect of an adaptive-density filling structure on the mechanical properties of FDM parts with a variable cross-section. Materials 2022;15:8746. https://doi.org/10.3390/ma15248746.
[29] Yi L, Mertes J, Klar M, Ghansiyal S, Fei C, Glatt M, et al. A new gradient infill design method for material extrusion using density-based topology optimization and G-code extension. Manuf Lett 2023;37:21–5. https://doi.org/10.1016/j.mfglet.2023.06.003.
[30] Catana DI, Brus DI, Pop MA, Luca MA. Influence of 3D printing parameters on the mechanical properties for numerical simulation of the poly (lactic acid). Polymers (Basel) 2025:17. https://doi.org/10.3390/polym17172271.
[31] Aboelella MG, Ebeid SJ, Sayed MM. Layer combination of similar infill patterns on the tensile and compression behavior of 3D printed PLA. Sci Rep 2025;15:11759. https://doi.org/10.1038/s41598-025-94446-8.
[32] Xia L, Ma G, Wang F, Bai G, Xie YM, Xu W, et al. Globally continuous hybrid path for extrusion-based additive manufacturing. Autom Constr 2022;137:104175. https://doi.org/10.1016/j.autcon.2022.104175.
[33] Bi M, Xia L, Tran P, Li Z, Wan Q, Wang L, et al. Continuous contour-zigzag hybrid toolpath for large format additive manufacturing. Addit Manuf 2022;55:102822. https://doi.org/10.1016/j.addma.2022.102822.
[34] Al Khalil M, Belkebir H, Lebaal N, Demoly F, Roth S. A biomimetic design method for 3D-printed lightweight structures using L-systems and parametric optimization. J Comput Des Eng 2023;10:2001–16. https://doi.org/10.1093/jcde/qwad046.
[35] Podroužek J, Marcon M, Ninčević K, Wan-Wendner R. Bio-inspired 3D infill patterns for additive manufacturing and structural applications. Materials 2019;12:499. https://doi.org/10.3390/ma12030499.
[36] Öztürk FH, Temiz A, Pehlivan F. Numerical and experimental investigation of failure mechanisms in additively manufactured multimaterial triply periodic minimal surface polymer cellular materials. Adv Eng Mater 2026. https://doi.org/10.1002/adem.202502387.
[37] Primo T, Calabrese M, Del Prete A, Anglani A. Additive manufacturing integration with topology optimization methodology for innovative product design. Int J Adv Manuf Technol 2017;93:467–79. https://doi.org/10.1007/s00170-017-0112-9.
[38] Kubalak JR, Root NJ, Wicks AL, Williams CB. Improving mechanical performance in material extrusion parts via optimized toolpath planning. Addit Manuf 2024;80:103950. https://doi.org/10.1016/j.addma.2023.103950.
[39] Sadeghieh M, Saelzer J, Hosseini A, Kishawy H, Biermann D. Look-ahead stress-oriented trajectory planning to improve the strength of fused filament fabricated parts. CIRP J Manuf Sci Technol 2025;61:249–67. https://doi.org/10.1016/j.cirpj.2025.06.017.
[40] Yan G, Xu J, Xiao T, Zhang G, Jiang X, Sun Y. Principal stress direction-aware streamlined printing path planning for fused filament fabrication. Compos Part A Appl Sci Manuf 2025;190:108642. https://doi.org/10.1016/j.compositesa.2024.108642.
[41] Kipping J, Nettig D, Schüppstuhl T. Looping: load-oriented optimized paths in non-planar geometry. Addit Manuf 2024;94:104426. https://doi.org/10.1016/j.addma.2024.104426.
[42] Liu T, Yuan S, Wang Y, Xiong Y, Zhu J, Lu L, et al. Stress-driven infill mapping for 3D-printed continuous fiber composite with tunable infill density and morphology. Addit Manuf 2023;62:103374. https://doi.org/10.1016/j.addma.2022.103374.
[43] Wang T, Li N, Link G, Jelonnek J, Fleischer J, Dittus J, et al. Load-dependent path planning method for 3D printing of continuous fiber reinforced plastics. Composites Part A 2021;140:106181. https://doi.org/10.1016/j.compositesa.2020.106181.
[44] Edwards R, Clemon L. Improving the strength of fused filament fabrication parts by non-planar alignment of material extrusion with stress vectors. In: 2024 IEEE 20th international conference on automation science and engineering (CASE). IEEE; 2024. p. 2249–55. https://doi.org/10.1109/CASE59546.2024.10711587.
[45] Guidetti X, Balta EC, Nagel Y, Yin H, Rupenyan A, Lygeros J. Stress flow guided non-planar print trajectory optimization for additive manufacturing of anisotropic polymers. Addit Manuf 2023;72:103628. https://doi.org/10.1016/j.addma.2023.103628.
[46] Zappino E, Filippi M, Pagani A, Petiti M, Carrera E. Experimental and numerical analysis of 3D printed open-hole plates reinforced with carbon fibers. Composites Part C: Open Access 2020;2:100007. https://doi.org/10.1016/j.jcomc.2020.100007.
[47] Ghanbari A, Ayatollahi MR, Choupani N, Torabi AR. Tensile fracture of blunt V-notches in rectangular plates additively manufactured from acrylonitrile butadiene styrene with different raster angles. Eng Fail Anal 2024;164:108670. https://doi.org/10.1016/j.engfailanal.2024.108670.
[48] Torabi AR, Shahbaz S, Ayatollahi MR. Fracture assessment of U-notched diagonally loaded square plates additively manufactured from ABS with different raster orientations. Eng Struct 2023;292:116537. https://doi.org/10.1016/j.engstruct.2023.116537.
[49] Adibeig MR, Saeimi-Sadigh M-A, Vakili-Tahami F, Karimani MR, Marami G. Quasi-static simulation and fatigue life estimation of fused filament fabrication of polylactic acid specimens using finite element method. J Manuf Process 2023;106:202–13. https://doi.org/10.1016/j.jmapro.2023.09.071.
[50] Khosravani MR, Reinicke T. Mechanical strength of 3D-printed open hole polymer plates. Procedia Struct Integrity 2022;41:664–9. https://doi.org/10.1016/j.prostr.2022.05.075.
[51] Yamamoto K, Luces JVS, Shirasu K, Hoshikawa Y, Okabe T, Hirata Y. A novel single-stroke path planning algorithm for 3D printers using continuous carbon fiber reinforced thermoplastics. Addit Manuf 2022;55:102816. https://doi.org/10.1016/j.addma.2022.102816.
[52] Kalyoncu E, Temiztaş BA, Bolat B, Kaya AC. Mechanical performance and structural integrity of 3D-printed Polylactic acid in tensile testing: influence of hole fabrication technique and process parameters. Latin American Journal of Solids and Structures 2026:23. https://doi.org/10.1590/1679-7825/e8775.
[53] Mazarbhuiya RM, Veeman D. Tensile performance of 3D-printed PLA material with conventionally drilled and additively fabricated holes. Prog Addit Manuf 2026. https://doi.org/10.1007/s40964-025-01483-w.
[54] Verma P, Ubaid J, Schiffer A, Jain A, Martínez-Pañeda E, Kumar S. Essential work of fracture assessment of acrylonitrile butadiene styrene (ABS) processed via fused filament fabrication additive manufacturing. Int J Adv Manuf Technol 2021;113:771–84. https://doi.org/10.1007/s00170-020-06580-4.
[55] Krajangsawasdi N, Hamerton I, Woods BKS, Ivanov DS, Longana ML. Open hole tension of 3D printed aligned discontinuous composites. Materials 2022;15:8698. https://doi.org/10.3390/ma15238698.
[56] Kargar E, Hosseini-Taklimi S-A, Ghasemi-Ghalebahman A. Fracture behavior of sustainable wood and PLA composites fabricated by fused deposition modeling using essential work of fracture. Sci Rep 2025;15:34929. https://doi.org/10.1038/s41598-025-18766-5.
[57] Yap T, He Z, Wang Z, Tamijani A, Tehrani M. Experimental investigation and validation of strength-based topology and fiber path optimization in additively manufactured continuous fiber reinforced composites. Addit Manuf 2024;89:104274. https://doi.org/10.1016/j.addma.2024.104274.
[58] Torabi AR, Shahbaz S, Ayatollahi MR. Tensile fracture prediction of 3D-printed V-notched PLA specimens: application of VIMC-MEMC in conjunction with brittle fracture criteria. Eng Fract Mech 2024;310:110497. https://doi.org/10.1016/j.engfracmech.2024.110497.
[59] Xia L, Lin S, Ma G. Stress-based tool-path planning methodology for fused filament fabrication. Addit Manuf 2020;32:101020. https://doi.org/10.1016/j.addma.2019.101020.
[60] Zhang H, Yao Y, Ma Y, Lackner M, Jiang Y. A 3D printing tool-path generation strategy based on the partition of principal stress field for fused filament fabrication. Int J Adv Manuf Technol 2022;122:1719–35. https://doi.org/10.1007/s00170-022-09957-9.
[61] Schiele A, Tesari I, Greiner C. Biomechanical optimization of printing paths in fused filament fabrication. Mater Today Commun 2026;50:114621. https://doi.org/10.1016/j.mtcomm.2026.114621.
[62] Zhang H, Li A, Wu J, Sun B, Wang C, Yang D. Effectiveness of fibre placement in 3D printed open-hole composites under uniaxial tension. Compos Sci Technol 2022;220:109269. https://doi.org/10.1016/j.compscitech.2022.109269.
[63] Wang G, Wang F, Guan S, Fu R, Wang H, Lei Y. A new path planning strategy driven by geometric features and tensile properties for 3D printing of continuous fiber reinforced thermoplastic composites. Compos Part B Eng 2025:288. https://doi.org/10.1016/j.compositesb.2024.111885.
[64] Stelmaszek M, Zdroik P, Porter-Sobieraj J. Automated 3D-printing path generation for parts with holes using continuous fibre filament. Virtual Phys Prototyp 2024:19. https://doi.org/10.1080/17452759.2024.2402871.
[65] Hou Z, Tian X, Zhang J, Zheng Z, Li Z, Li D, et al. Optimization design and 3D printing of curvilinear fiber reinforced variable stiffness composites. Compos Sci Technol 2021;201:108502. https://doi.org/10.1016/j.compscitech.2020.108502.
[66] Tawfik H, Goldsmith P. A multi-layer approach for additive manufacturing of continuous fiber composites. Polym Compos 2025;46:3623–35. https://doi.org/10.1002/pc.29195.
[67] Li N, Link G, Wang T, Ramopoulos V, Neumaier D, Hofele J, et al. Path-designed 3D printing for topological optimized continuous carbon fibre reinforced composite structures. Compos Part B Eng 2020;182:107612. https://doi.org/10.1016/j.compositesb.2019.107612.
[68] https://www.prusa3d.com/; 2026.
[69] ISO 527-1. Plastics — Determination of tensile properties — Part 1: General principles. 2019.
[70] https://eu.elegoo.com/collections/filaments/products/pla-filament-1-75mm-colored-1kg; 2026.
[71] https://www.shimadzu.eu/products/materials-testing/uni-ttm/autograph-precision-universal-tester/index.html; 2026.
[72] https://www.correlatedsolutions.com/vic-3d/; 2026.